h-BN/metal-oxide interface grown by intercalation: A model system for nano-confined catalysis

J. Trey Diulus,[1,2] Zbynek Novotny,[1,2†] Nanchen Dongfang,[3] Jan Beckord,[1] Yasmine Al-Hamdani,[3,4] Nicoló Comini,[1,2] Matthias Muntwiler,[2] Matthias Hengsberger,[1] Marcella Iannuzzi,[3] Jürg Osterwalder[1]*

[1]Department of Physics, University of Zürich; 8057 Zürich, Switzerland

[2]Swiss Light Source, Paul Scherrer Institute; 5232 Villigen PSI, Switzerland

[3]Department of Chemistry, University of Zürich; 8057 Zürich, Switzerland

[4]Department of Earth Sciences, University College London, London WC1E 6BT, United Kingdom

KEYWORDS: h-BN; intercalation; Cu_2O; 2D cover; APXPS

ABSTRACT

Deposition of 2D materials onto catalyst surfaces is known to alter the adsorption energies of active sites due to the nanoconfinement effect. Traditionally, these 2D catalyst heterostructures were prepared by depositing a 2D material onto a pristine metallic surface. Preparing well-defined 2D monolayers instead on metal-oxide surfaces is challenging, although possible *via* O_2 intercalation by oxidizing a metal substrate underneath. Several studies demonstrate this

intercalative behavior of 2D covers, however, without preparation of ordered structures, which are imperative for defining fundamental reaction mechanisms in confined space. We report the successful preparation and characterization of a well-defined, ultrathin cuprous oxide-like film grown in-between h-BN and Cu(111). The confined surface oxide adopts a "Cu_2O-like" structure resembling the well-studied "44" Cu_2O structure, although the oxidation temperature is surprisingly lower than its uncovered oxide counterpart and the h-BN layer remains intact following oxidation. Our experimental results, backed by theoretical simulations, outline the development of a heterostructure with a h-BN/metal-oxide interface as a model system, utilizing a preparation method likely transferable to a wide range of 2D/metal heterostructures, and opening the door to new catalyst designs.

MAIN TEXT

Introduction

The activity and selectivity of a catalytic reaction is strongly dependent on the presence of specific active sites at the catalyst surface, the binding strength of adsorbates to these sites, and the structural environment around the bound adsorbates. Confining active sites in porous structures is a promising route towards enhancing catalytic performance, namely with zeolites,[1] metal-organic frameworks,[2] and carbon nanotubes.[3-4] While these systems represent confinement in zero and one dimensions, confinement in two dimensions is also possible *via* intercalation of reactants between weakly-interacting two-dimensional (2D) layers.[5-8] Over the last decade, monolayers of 2D materials grown on metal surfaces have become used as model systems to study such 2D-confined catalysis because they can be prepared in a structurally well-defined form and can be characterized in great detail by surface science techniques, providing solid

experimental reference data for theoretical studies.[9-11] Although these and many other prior studies with metal substrates are pioneering for 2D-confined catalysis studies,[12-15] several metals have been shown to be more catalytically active in their oxidized state.[16] More specifically, certain metals are catalytically active towards oxidation reactions due to the formation of a surface oxide, where these reactions generally follow Mars van Krevelen mechanisms.[17] Thus, to further understand confined chemical reactions, we must prepare model systems with a h-BN/metal-oxide interface (h-BN/MOx).

Much of the prior studies in 2D-confined catalysis utilize graphene (Gr),[13-14, 18] particularly for CO oxidation on Gr/Pt(111), which can be significantly enhanced due to weaker CO adsorption energies compared to the bare Pt(111) surface.[19] More recently, theoretical calculations have suggested Gr "pores" formed by sporadic holes in the Gr lattice approximately three hexagons wide can further tune the selectivity by allowing intercalation of specific molecules while preventing others.[20] However, using Gr makes surface characterization by electron spectroscopy slightly more complicated due to unavoidable adventitious species, while adding further complexity if trying to also study reaction mechanisms. Alternatively, hexagonal boron nitride (h-BN) is another interesting 2D material exhibiting a large bandgap (~6 eV), thus electrically insulating, while being more chemically robust than Gr at high temperatures, which is necessary for chemical reactions.[21-22] A single atomically thick h-BN monolayer can be grown on metal surfaces in a similar way as Gr,[23] and such systems were already suggested as potential highly selective, corrosion-resistant, "nano-reactor" catalyst systems studied in view of molecule intercalation[5, 8, 24] and confined catalysis,[7, 25] exhibiting similar intercalation behavior to their Gr counterparts. While monolayer 2D materials typically form strong intralayer bonds, the weak interactions with an underlying substrate allow for the intercalation of molecular species. This can lead to changes in active surface sites and stimulate chemical reactions in confined space.[10]

h-BN/Cu(111) is a prime system for these studies due to the weak interaction with the h-BN layer, leading to a Van-der-Waals gap of roughly 3 Å.[26]

CVD growth of h-BN on metallic surfaces is well reported,[23] however, direct growth on metal oxides, and many other insulating materials, is much more challenging.[27-28] Any high pressure/high temperature reaction for h-BN growth utilizes highly reducing chemicals (borazine, ammonia borane, triethylboron, etc.) that react with the oxide surface, or lead to defective h-BN layers compared to growth on metal surfaces.[23, 28] Metal etch and exfoliation transfer techniques are one common route to form a h-BN/MOx,[29] but these methods do not provide the same quality compared to direct deposition under vacuum conditions. Transferred h-BN can form highly defective 2D layers, either due to incomplete or multi-layers formed.[28] Contamination is also an issue both from adventitious species that can be trapped during transfer or residual substrate present following etching if wet transferred.[28, 30] These transferred heterostructures may be suitable for many material science applications, but are not ideal for studying fundamental reaction mechanisms, where it is imperative to have a homogeneous surface with known and well-defined structure. Other vacuum-based techniques, like sputter deposition and additional physical vapor techniques, tend to create multilayer films that would significantly limit intercalative reactions.[31] One potential solution is to transfer h-BN with a "stamp" approach, demonstrated by Wang et al., for clean transfer of h-BN on SiO_2.[32] However, this method is more suitable for transfer to bulk oxides where the goal is to encapsulate an oxide surface with h-BN compared to studying reactions at the interface. A more reactive surface oxide thin film (~0.4 nm) would likely not survive the "stamp" process, nor would an ordered interfacial oxide layer be expected. Instead, in this work we explore forming a stacked heterostructure by intercalating molecular oxygen through h-BN and oxidizing the underlying metal substrate to create a confined h-BN/MOx.[33] This, combined with thermal annealing, results

in the oxidation of the top few layers of the metallic substrate underneath. Additionally, our results demonstrate that, within a narrow window of oxidizing conditions, the formed oxide is highly ordered with a structure close to that of cuprous oxide.

Cuprous oxide (Cu_2O) has been demonstrated as an environmentally friendly, inexpensive, Earth-abundant metal oxide material effective for many catalysis applications.[34-36] Cu_2O is one of the most common corrosion products of Cu, thus studying reactions on Cu_2O surfaces is vital for understanding copper-based catalysis in general. The most energetically favorable Cu_2O surface is the O-terminated $Cu_2O(111)$, containing coordinatively saturated and unsaturated ions of both copper and oxygen.[35] CO can adsorb on both O and Cu atoms, providing two pathways towards CO oxidation, although adsorption on Cu and reaction with a neighboring oxygen through a Mars–van Krevelen mechanism is the most energetically favorable pathway.[34, 37] The high activity towards complete CO oxidation has previously been observed for Cu_2O nanoparticles at temperatures as low as 250 °C, although O_2 is required to replenish oxygen vacancies as CO_2 is formed.[34] The partial O_2 pressure is critical, however, as overoxidation will lead to the formation of CuO.[34, 36] h-BN has been suggested as a potential corrosion resistant layer for Cu,[38-39] although h-BN/Cu has still been shown to intercalate O_2 and oxidize the Cu substrate.[40-41] However, when h-BN is present, overoxidation to CuO is largely reduced.[39] Kidambi et al. shows clear evidence of oxygen intercalation from electron microscopy images, that eventually disintegrates the h-BN layer once annealed to 700 °C.[41] In our case, the goal is to utilize the parameter space of the formed intercalated oxide prior to h-BN etching, where the h-BN layer can assist in preventing overoxidation, while still allowing oxidation reactions to take place on the Cu surface *via* intercalation at conditions that exposed Cu_2O would typically be unstable.[38]

Furthermore, the h-BN can act as a support to confine the range of motion for adsorbates.[42] For example, if a molecule adsorbs to an exposed $Cu_{2-x}O$ surface under finite temperature, the molecule can easily desorb without reacting with any surface oxide. However, with the h-BN layer present, the probability of an adsorbed molecule splitting and reacting with a neighboring O atom is expected to increase. Liang et al. provide evidence of this nanoconfinement effect through molecular dynamics simulations that show confined H_2O molecules in a carbon nanotube exhibit slightly weaker hydrogen bonding than bulk molecules.[43] Utilizing h-BN nanosheets as a support for anchoring Cu_2O clusters is similar in concept to our reported heterostructure,[42] but instead our heterostructure is the reverse architecture that confines an entire $Cu_{2-x}O$ layer, allowing for further tuning of the reaction mechanism. Still, we must emphasize that once the h-BN monolayer is destroyed, the substrate is rapidly oxidized to a thick oxide film, displaying a macroscopic change seen in figure S5e. Scardamaglia et al. have seen this identical behavior for h-BN deposited on Cu foils, where the h-BN layer survives for a specific period of time after forming a $Cu_{2-x}O$ layer underneath.[40] This time not only varies with oxygen exposure conditions, but also with h-BN quality, especially with wrinkles in the case of foils, and thus requires a dedicated recipe to avoid removal of h-BN and simultaneously take advantage of the catalytic properties of the $Cu_{2-x}O$ surface oxide.

In this study, we prepared a h-BN/MOx *via* intercalation of molecular oxygen through an h-BN monolayer to oxidize the underlying Cu(111) substrate. We used ambient pressure x-ray photoelectron spectroscopy (APXPS), x-ray photoelectron diffraction (XPD), x-ray absorption spectroscopy (XAS), low-energy electron diffraction (LEED), Auger electron spectroscopy (AES), and scanning tunneling microscopy (STM) to experimentally characterize the resulting heterostructure. APXPS was performed to determine the oxidation state of the $Cu_{2-x}O$ film and track the presence of h-BN with respect to O_2 pressure and sample temperature. XAS was

utilized as a complimentary tool to determine the Cu oxidation state for each reaction condition, and to ensure the h-BN monolayer remained intact. STM was used to obtain topographical measurements of the surface, while calculations using density functional theory (DFT) provided a model structure. The comparison of simulated STM images and simulated XAS to experimental data was used to validate the assignment of the structural features at the interface. Altogether, we report the ordered h-BN/$Cu_{2-x}O$/Cu(111) heterostructure that represents a model "nano-reactor" catalyst system.

Results and Discussion

In order to fully define the intercalative oxidation parameter space of h-BN/Cu(111), APXPS was utilized at multiple temperature and O_2 partial pressure conditions. A detailed description of the time-resolved temperature and pressure dependent experiments is presented in the supporting information (SI). After several attempts, a recipe was defined where an h-BN/Cu(111) sample was exposed to oxygen for ~5-40 min at p_{O2} = 1 mbar and 150 °C to obtain an ordered Cu_2O-like oxide, while the h-BN layer remained intact. The variable time defines the formation of an ordered oxide before destruction of the h-BN layer. The exposure time for development of the oxide varies with the number of defects and BN grain boundaries at the surface, along with residual carbon contamination above the h-BN that will react with the oxygen ambient. When growing h-BN, several factors like chamber background pressure (specifically H_2 partial pressure), borazine vapor pressure, sample temperature, sample cleanliness, and surface roughness all impact the amount of grain boundaries and defects that form.[23] It is well established that atom or molecular intercalation occurs at defects and grain boundaries of h-BN layers,[44] while a defect-free h-BN monolayer is virtually impenetrable for

adsorbates but practically impossible to prepare. In figure S3, we highlight a few h-BN grain boundaries seen from STM for our preparation to show the defect density of our monolayer. Oxidation of Cu foils with h-BN has shown evidence of termination at Cu_2O, compared to CuO for unprotected bare Cu foils after ~100 hours of exposure to air at 250 °C.[39] We found the best preparation of the h-BN/$Cu_{2-x}O$/Cu(111) heterostructure in terms of structural coherence, prior to the formation of any CuO, to be the one following the "5 min" oxidation exposure protocol described further in the SI. Therefore, the focus of the main text will be the characterization of this "5 min" oxide.

Low-temperature STM provides topographical information of our heterostructure, shown in Figure 1. STM images of the sample surface were obtained using a negative sample bias of -2.5 V and a tunneling current of 200 pA acquired at 78 K. In this case, we probe the filled Cu_d states of the surface oxide, where we see atomic resolution for the grown oxide film in Figure 1a and b corresponding to 3 × 3 nm^2 and 25 × 25 nm^2 area, respectively. Using the high-resolution 25×25 nm^2 image, we determine a diffraction pattern from the STM image by applying a Fast Fourier Transform (FFT), shown in Figure 1c. A further description of this analysis is provided in the SI. The FFT pattern is compatible with a 6-fold symmetric pattern, which strongly resembles the hexagonal structure in the LEED image collected at 40 eV shown in Figure 1d. The unit cell is highlighted by a teal rhombus in Figure 1a, 1c and 1d. A closer look at the comparison of FFT and LEED is depicted in figure S3. The unit cell can be determined from the STM images by overlaying a grid on top of the repeated structure displayed in Figure 1a, corresponding to 10.2 × 10.2 $Å^2$ rhombus with an angle of 60°. These dimensions were used to draw a unit cell in the LEED, matching well with the calibrated distance of the diffraction spots and further highlighted in figure S2 and figure S3. This larger unit cell corresponds to the

chemisorbed oxide forming a (4×4) overlayer on the surface, comprising of four times the length between two FCC sites of the Cu(111) surface.

Using the (4×4) unit cell deduced from STM and LEED experiments, we built a model of the heterostructure with a periodic slab shown in Figure 2. The slab consists of four components: (i) 4 layers of Cu atoms, terminating in a 4×4 Cu(111) surface, (ii) a single $Cu_2O(111)$ tri-layer designated as a surface oxide (O-Surf) later in the text, from which all unsaturated Cu atoms are removed ($Cu_{2-x}O(111)$) and we distinguish between lower (O_l closer to Cu(111)) and upper (O_u) oxygen atoms, (iii) a chemisorbed layer of O atoms in the available Cu_{fcc} sites designated as O-Chem, located beneath the centers of $Cu_{2-x}O(111)$ honeycombs, (iv) and on top a (8×8) h-BN layer placed along the same hexagonal symmetry direction as the underlying Cu(111) substrate. All atoms of the model slab have been relaxed by DFT to obtain an optimized stable structure. This heterostructure has some resemblance with the honeycomb-like oxidation cluster suggested by Yang et al.[45] of a similar oxide layer prepared on bare Cu(111) (without h-BN). Note that we considered other possible surface structures that satisfy the symmetry observed in experiment, for instance with chemisorbed O atoms at Cu_{hcp} and Cu_{top} sites. Among the tested structures, the one described above turns out to be the most energetically favorable.

It is imperative the h-BN remains intact during oxidation, otherwise intercalative oxidation will not take place and lead to overoxidized patches on the surface. Therefore, we employed several characterization techniques to ensure we did not alter or destroy the h-BN layer. With XAS, we can probe both chemical state information and the electronic structure of the atoms present, providing a basis for the quality of the h-BN layer. The B and N K-edges resulting from h-BN display peaks from both sp^2 or sp^3 hybridized bonds, along with additional peaks corresponding to grain boundaries and vacancies.[46] The N and B K-edges shown in Figure 3a and 3b, respectively, resemble high-resolution XAS data for h-BN monolayer films, showing

both the σ* and π* peaks reported in the literature.[46-47] Additionally, the B and N K-edges after oxidation are nearly identical to the freshly prepared h-BN sample, with the sole exception of a small pre-edge in the N K-edge that disappears after oxidation (highlighted with a double arrow in Figure 3a. This pre-edge corresponds to the orbital mixing of the unoccupied π* orbitals with the delocalized Cu 4s,p_z bands of the substrate.[48] Following oxidation, the pre-edge disappears because the surface oxide has no such bands.

The σ* and π* peaks for both the N and B K-edge remain almost identical, suggesting the hexagonal sp^2 bonding structure of the h-BN remains intact. Additionally, the total intensity does not decrease relative to monolayer h-BN prior to oxidation, thus no loss of B or N takes place. This is consistent with the LEED and AES measurements collected on the same spot presented in figure S1, further demonstrating the h-BN layer remains intact and coexists with the copper oxide structure. LEED was acquired in 5 different spots on the surface with ~300 μm diameter electron beam size, while similarly XPS was also taken in 2-3 spots for different spot sizes to ensure the h-BN coverage and surface oxidation were homogenous and consistent. We also scanned the sample with STM in several spots seeing the same structure over ~0.5 mm^2 corresponding roughly to the size of the x-ray/e-beam spot. This strongly highlights the homogeneity of the heterostructure over large length scales.

The O K-edge in Figure 3c shows evidence of at least two oxidation states with a pre-edge at ~529.5 eV, along with a more intense edge at ~532 eV. The latter value is characteristic of Cu_2O,[49-50] while a lower energy pre-edge (~530 eV) generally corresponds to CuO.[49] However, we know from the Cu L-edge in Figure 3d that we do not have CuO as the L_2 peak would shift to the lower energy of ~930 eV due to d_9 states being excited in CuO, which should create a pre-edge just below the L_3 peak.[49, 51] While XAS from TEY is typically thought to be more "bulk" sensitive, using soft x-rays can actually be very surface sensitive (< 2 nm)[52] and

should demonstrate some evidence of a peak in the Cu L edge that corresponds with the O K-edge if CuO is present. Therefore, the lower energy peak represents undercoordinated chemisorbed O, while the higher energy peak corresponds to a Cu_2O-like structure. Gurevich *et al.* collected XAS for a Cu(100) surface oxide after exposure to 30 Langmuir (L) of O_2,[49] which displays remarkable similarity to the spectra presented in Figure 3c. Furthermore, in figure S8, we display the O K-edge for a $Cu_2O(111)$ reference with a (1×1) bulk-terminated surface and also show the oxidation progression starting from a bare h-BN/Cu(111) sample where intensity of the peak located at 532 eV increases with increasing oxidation. This is identical for the ordered oxide and this intensity increase of the 532 eV peak was also seen for a sample oxidized for 35 min in figure S11, while the pre-edge intensity remains the same as the 5 min oxidation. Simulated peak positions from DFT shown in figure S11f for each O configuration in the surface oxide also agree with this description and highlight the contribution of each peak separately.

While XAS provides useful information of the oxidized binding structure, XPS is needed for obtaining the chemical state information of the h-BN/$Cu_{2-x}O$/Cu(111) sample in comparison to the pristine h-BN/Cu(111) system. Based on several preparations using different oxidation conditions, we find that the O 1s spectrum in Figure 4a can be consistently fitted with five peaks. We assign the lowest binding energy (BE) peak (~529.1 eV, blue curve) to an undercoordinated chemisorbed oxygen species, agreeing with the above assignment of the pre-edge peak in the XAS data. This is also seen in literature for Cu_2O thin films as well as for undercoordinated surface O in bulk Cu_2O, respectively.[35, 53] The middle peak in the O 1s spectrum (~529.5 eV, red curve) is assigned to a Cu_2O-like surface oxide. A third oxide peak is seen at 530.4 eV (green curve), which represents $Cu_{2-x}O$ clusters. It is well known that Cu oxidizes by forming island facets,[54] resembling a O_3-Cu pyramid, which would form in our case at h-BN grain boundaries. Wiame et al. additionally show oxide cluster formation on the Cu surface from STM,[55] largely

resembling the clustering that we see for longer oxidized samples, such as the "35 min" sample shown in figure S13. As we continue to oxidize our sample, more clusters form in increasing sizes at these grain boundaries, causing this 530.4 eV peak to increase, shown in figure S11. We also see from the angle dependent XPS figure S12d that the 530.4 eV peak for the clusters at 90° has a larger ratio relative to the surface oxide peak at grazing emission, confirming these clusters are at the topmost surface. Moreover, the clusters have heights of ~2-3 nm above the surface, as determined from STM line profiles, which explains why the more bulk sensitive spectra taken with 1500 eV photon excitation energy also show an increase of the cluster peak relative to the chemisorbed and surface oxide peaks. A depiction of this "shadowing" effect is given in figure S13. This oxidation mechanism, where a peak at ~530.4 eV increases with increasing oxygen exposure has also been seen for APXPS exposures of a bare Cu(111) surface exposed to O_2.[56] Finally, the higher BE peak seen at ~531.6 eV is a result of adventitious contamination, most likely carbonaceous oxygen. A small peak at ~533 eV is also present, which is most likely due to hydroxyl species due to preparing the sample in an unbaked ambient-pressure chamber.

The B 1s and N 1s spectra for the h-BN/Cu(111) system in Figure 4b and 4c both show a Gaussian peak at 190.5 eV and 398 eV, respectively, visible also after oxidation of the Cu(111) substrate although shifted by 0.3 eV to lower binding energy, which corresponds with the work function difference between Cu(111) and Cu_2O(111) surfaces.[57] Since h-BN is an insulating, weakly bonded layer above the substrate, the measured core level binding energies are referenced to the vacuum level and thus sensitive to changes in the substrate work function.[58] Both the B 1s and N 1s additionally have a shoulder on the high BE side located approximately 0.6 eV above the main peak. These shoulders correspond to defects in the h-BN lattice, that could be related to either B or N vacancies, or H adsorption.[26] Overall, the XPS for B and N 1s

before and after oxidation provides further evidence that the h-BN layer remains intact while oxidizing the substrate.

The C 1s spectrum, displayed in Figure 4e, initially shows only adventitious carbon, some of which becomes oxidized during the O_2 intercalation experiment leading to an additional higher binding energy peak. Again, the same 0.3 eV shift to lower BE present in B 1s and N 1s is also seen in the C 1s, due to the carbon species sitting on top of the h-BN. There is a slight increase in total carbon signal at the surface, which is expected as the sample must be prepared and transferred between two vacuum systems *via* a vacuum suitcase. However, the carbon coverage grows from 0.09 to 0.14 ML as evaluated by comparison with the Cu 3p peak, which is not expected to significantly impact the experiment.

The oxidation of Cu has been extensively explored with theoretical studies combined with traditional surface science experiments to elucidate the oxidation mechanism and identify potential intermediate oxides.[45, 54, 56, 59-60] Notably, there is a characterization gap that exists in that no known study provides combined STM and LEED analysis for the same surface oxide structures, with or without h-BN present. Our attempt to provide both image and diffraction characterizations in a comprehensive model will assist future studies of Cu surface oxidation. Most interestingly, our results show the ability to form a well-ordered surface oxide at significantly lower temperatures than the "29" and "44" oxides would form when exposing a bare Cu(111) surface with no h-BN cover (generally requiring 280-500 ºC annealing temperatures, in contrast with 150 °C needed with the h-BN cover). Theoretical studies suggest the formation of a (4×4) oxide should be possible at low temperatures,[61] but our attempts to obtain an ordered oxide without an h-BN cover at <200 ºC were unsuccessful. Forming an ordered structure at low temperatures strongly suggests that the nano-confinement effect of the h-BN monolayer influences the formation of the $Cu_{2-x}O$-like thin film, increasing the kinetics of

oxidation and thus requiring a lower temperature. The h-BN/Cu(111) surface was shown to be resistant to oxidation at p_{O2} = 1 mbar for ~8 hours when the temperature was either at or below 100 ºC (depicted in Figure S5). This opens the door for a potential reaction space ideal for molecular interactions with the confined Cu_2O film, while simultaneously limiting overoxidation.

Ultimately, we have provided a recipe along with extensive characterization and modeling for a model confined "nanoreactor" heterostructure that utilizes cheap and abundant materials, and standard gas-phase exposure processes. Several studies promoting the concept of confined catalysis have displayed a change in adsorption energies or diffusion barriers for intercalated species beneath a 2D monolayer.[12-14, 25] This nano-confinement effect with a h-BN/MOx is rather interesting for oxidation catalysis and potentially can influence the kinetics for reactions like CO oxidation that undergo a Mars-van Krevelen mechanism, for which Cu_2O surfaces have already been proposed as a promising material.[34, 37, 62] Our group has also looked at time resolved 2-photon photoemission (2PPE) experiments, highlighting that our confined trilayer oxide displays charge carrier dynamics that are remarkably similar to a bulk $(\sqrt{3}\times\sqrt{3})R30°$ $Cu_2O(111)$ surface.[63] Further development of the preparation parameters to reduce the number of oxygen vacancy defects in this oxide film may improve the surface quality enough to design a protected photocathode for photoelectrochemical water splitting,[63] also suggested by Mahvash et al..[38]

Conclusion

The recipe for the preparation of an ordered h-BN/MOx interface has been reported, formed *via* intercalation of O_2 underneath an h-BN layer and subsequent oxidation of the

underlying Cu(111) substrate. The Cu substrate is capable of withstanding oxidizing conditions for several hours and can form an ordered oxide with h-BN still intact if the temperature remains below 150 °C at an O_2 partial pressure of 1 mbar. This oxide preparation combined with our DFT calculations strongly suggests that the h-BN/Cu system can act as a promising oxidation catalyst through the controlled formation of a $Cu_{2-x}O$ surface oxide. This approach could likely be utilized on several substrates and 2D materials to build a wide range of heterostructures or tune the adsorption of specific probe molecules for different applications.

Having a model system is essential to study reactions in a confined space, which is what we demonstrate with this study of the preparation of an ordered h-BN/MOx heterostructure. Furthermore, the use of a 2D approach for confined catalysis with a well-ordered crystal substrate and formation of an ordered oxide provides a unique synergy with theoretical simulations, allowing for precise atomistic identification of the structure. Moving forward with molecular dynamic simulations allows for fundamental studies of molecular interactions that are imperative to identify reaction mechanisms, which is a knowledge gap that exists in 0D and 1D systems.

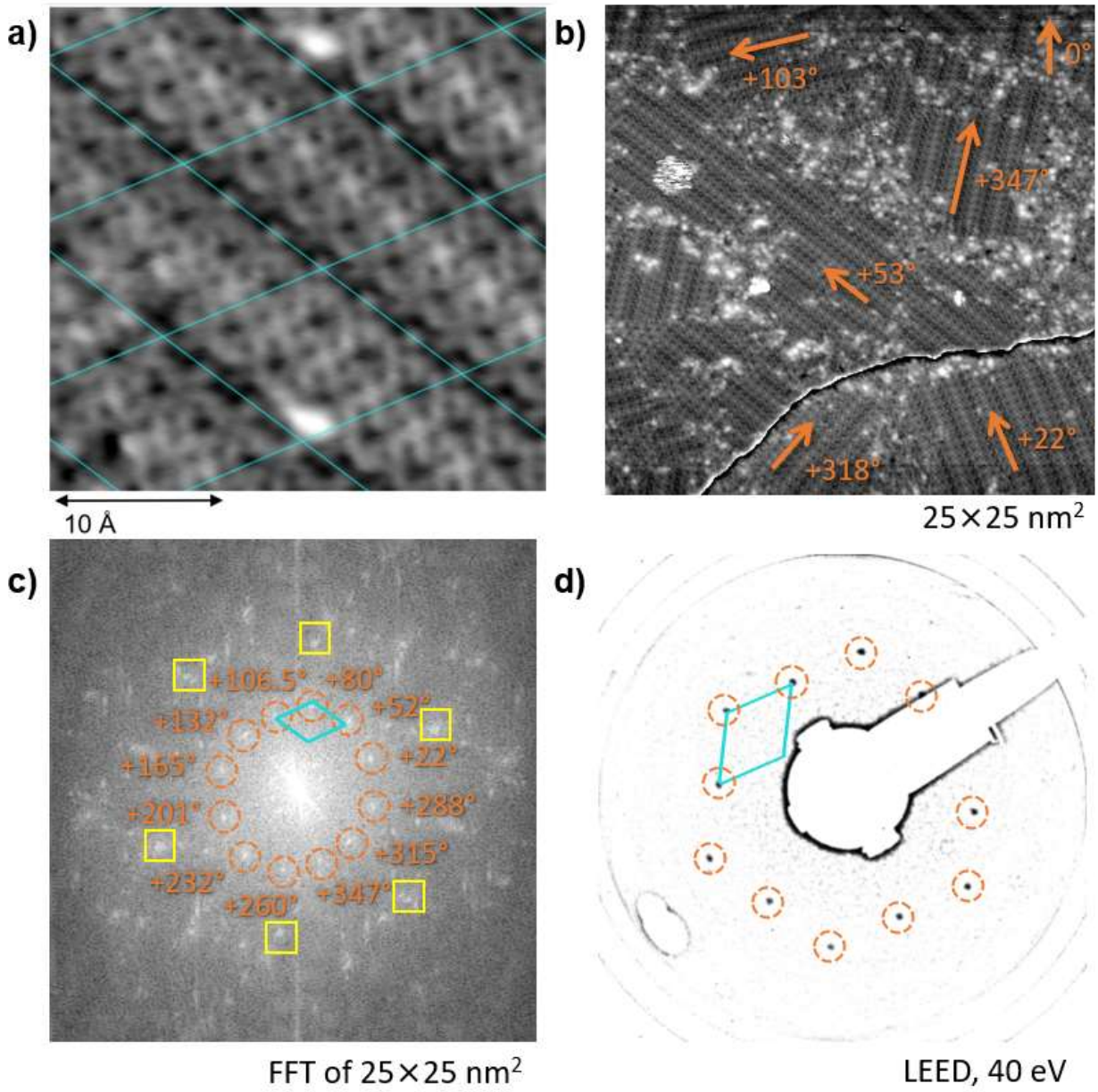

Figure 1. STM images using a -2.5 V sample bias and 200 pA current of the h-BN/$Cu_{2-x}O$/Cu(111) heterostructure for 3×3 nm^2 (a), and 25×25 nm^2 (b) after 5 min oxidation in p_{O2} = 1 mbar at 150 °C. A FFT analysis of the 25×25 nm^2 image is shown in (c). This corresponds with the LEED image (d) collected at 40 eV electron energy. The unit cell shown in (c) and (d) was determined to be a hexagonal unit cell of 10.2×10.2 $Å^2$ and an angle of 60°. The dark ridge in the bottom right of (b) is a Cu step edge, where the intensity was normalized to show the structure with the same height scaling on both sides of the step edge.

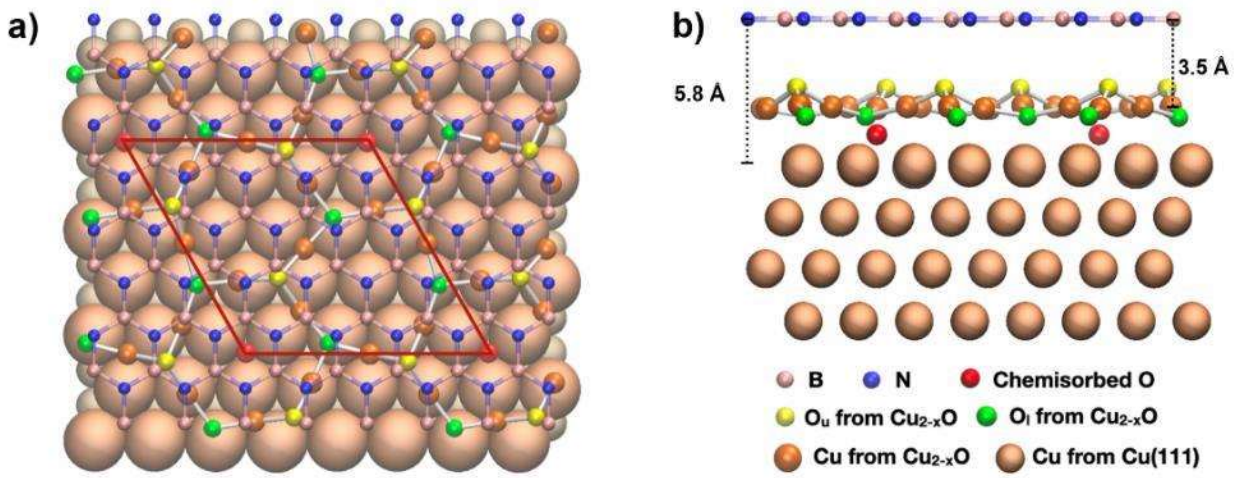

Figure 2. DFT-optimized slab model for the h-BN/$Cu_{2-x}O$/Cu(111) heterostructure with chemisorbed O atoms located under the $Cu_{2-x}O$ layer. a) top view and b) side view. The relaxed slab contains a distorted hexagonal $Cu_{2-x}O$(111) honeycomb structure. In the oxidation layer, a single unit cell (outlined in red) contains one chemisorbed O atom, three O_u atoms, and three O_l atoms.

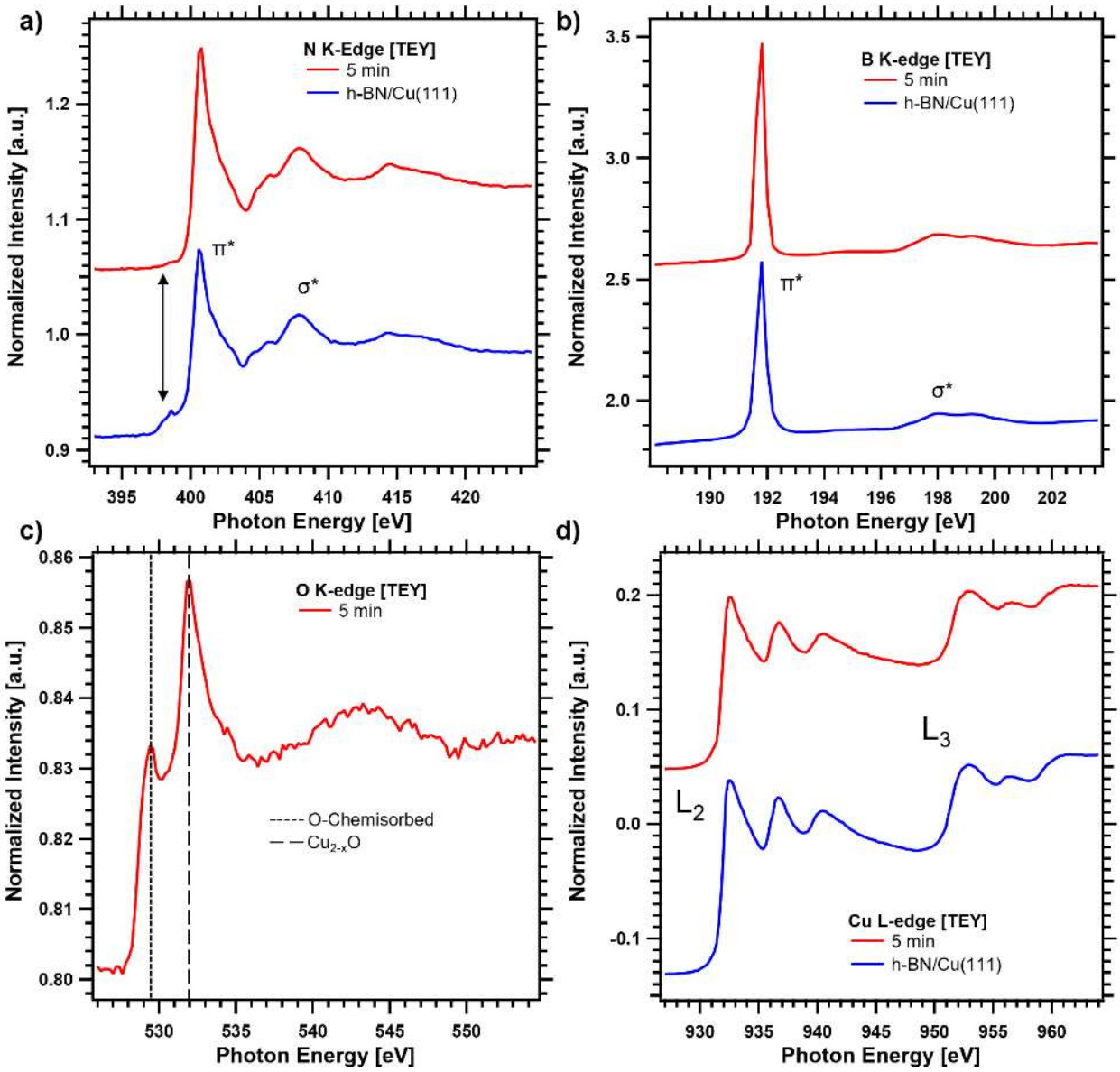

Figure 3. XAS of the h-BN/$Cu_{2-x}O$/Cu(111) after 5 min oxidation (red) and h-BN/Cu(111) prepared samples (blue) for the N K-edge (a), B K-edge (b), O K-edge (c), and Cu L-edge (d). The arrow highlights the disappearance of the pre-edge present in a pristine h-BN/Cu(111) sample.

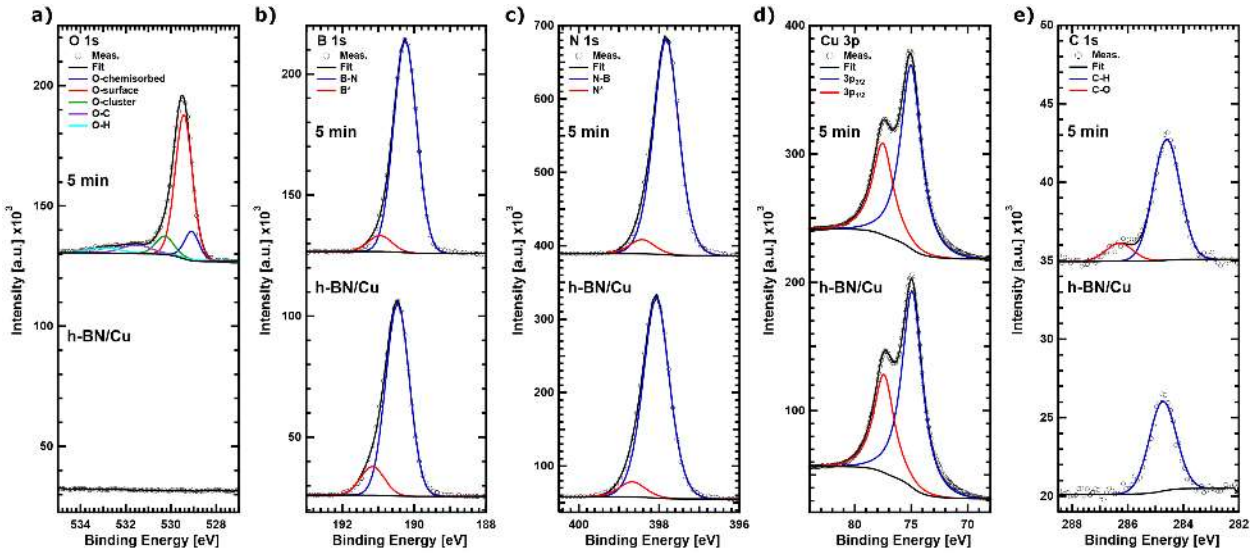

Figure 4. High-resolution XPS spectra of a well ordered h-BN/$Cu_{2-x}O$/Cu(111) heterostructure (top) after 5 min oxidation and a freshly prepared h-BN/Cu(111) sample (bottom) for O 1s (a), B 1s (b), N 1s (c), Cu 3p (d), and C 1s (e) core levels together with peak fits (solid lines) for the various contributions.

REFERENCES

1. Sastre, G.; Corma, A., The Confinement Effect in Zeolites. *Journal of Molecular Catalysis A: Chemical* **2009**, *305*, 3-7.
2. Choi, K. M.; Na, K.; Somorjai, G. A.; Yaghi, O. M., Chemical Environment Control and Enhanced Catalytic Performance of Platinum Nanoparticles Embedded in Nanocrystalline Metal–Organic Frameworks. *Journal of the American Chemical Society* **2015**, *137*, 7810-7816.
3. Serp, P.; Castillejos, E., Catalysis in Carbon Nanotubes. *ChemCatChem* **2010**, *2*, 41-47.
4. Pan, X.; Bao, X., The Effects of Confinement inside Carbon Nanotubes on Catalysis. *Accounts of Chemical Research* **2011**, *44*, 553-562.
5. Ma, C.; Park, J.; Liu, L.; Kim, Y.-S.; Yoon, M.; Baddorf, A. P.; Gu, G.; Li, A.-P., Interplay between Intercalated Oxygen Superstructures and Monolayer H -Bn on Cu(100). *Physical Review B* **2016**, *94*, 064106.
6. Makarova, A. A.; Fernandez, L.; Usachov, D. Y.; Fedorov, A.; Bokai, K. A.; Smirnov, D. A.; Laubschat, C.; Vyalikh, D. V.; Schiller, F.; Ortega, J. E., Oxygen Intercalation and Oxidation of Atomically Thin H-Bn Grown on a Curved Ni Crystal. *The Journal of Physical Chemistry C* **2018**, *123*, 593-602.
7. Zhang, Y.; Wei, M.; Fu, Q.; Bao, X., Oxygen Intercalation under Hexagonal Boron Nitride (H-Bn) on Pt(111). *Science Bulletin* **2015**, *60*, 1572-1579.
8. Preobrajenski, A. B.; Ng, M. L.; Vinogradov, N. A.; Vinogradov, A. S.; Lundgren, E.; Mikkelsen, A.; Mårtensson, N., Impact of Oxygen Coadsorption on Intercalation of Cobalt under the H-Bn Nanomesh. *Nano Letters* **2009**, *9*, 2780-2787.
9. Li, H.; Xiao, J.; Fu, Q.; Bao, X., Confined Catalysis under Two-Dimensional Materials. *Proceedings of the National Academy of Sciences* **2017**, *114*, 5930-5934.
10. Fu, Q.; Bao, X., Surface Chemistry and Catalysis Confined under Two-Dimensional Materials. *Chemical Society Reviews* **2017**, *46*, 1842-1874.
11. Shifa, T. A.; Vomiero, A., Confined Catalysis: Progress and Prospects in Energy Conversion. *Advanced Energy Materials* **2019**, *9*, 1902307.
12. Sutter, P.; Sadowski, J. T.; Sutter, E. A., Chemistry under Cover: Tuning Metal−Graphene Interaction by Reactive Intercalation. *Journal of the American Chemical Society* **2010**, *132*, 8175-8179.
13. Mu, R.; Fu, Q.; Jin, L.; Yu, L.; Fang, G.; Tan, D.; Bao, X., Visualizing Chemical Reactions Confined under Graphene. *Angewandte Chemie International Edition* **2012**, *51*, 4856-4859.

14. Zhou, Y.; Chen, W.; Cui, P.; Zeng, J.; Lin, Z.; Kaxiras, E.; Zhang, Z., Enhancing the Hydrogen Activation Reactivity of Nonprecious Metal Substrates Via Confined Catalysis Underneath Graphene. *Nano Letters* **2016**, *16*, 6058-6063.

15. Wang, S.; Feng, Y.; Yu, M. a.; Wan, Q.; Lin, S., Confined Catalysis in the *G*-C_3n_4/Pt(111) Interface: Feasible Molecule Intercalation, Tunable Molecule–Metal Interaction, and Enhanced Reaction Activity of Co Oxidation. *ACS Applied Materials & Interfaces* **2017**, *9*, 33267-33273.

16. Diebold, U.; Li, S.-C.; Schmid, M., Oxide Surface Science. *Annual Review of Physical Chemistry* **2010**, *61*, 129-148.

17. Lundgren, E.; Mikkelsen, A.; Andersen, J. N.; Kresse, G.; Schmid, M.; Varga, P., Surface Oxides on Close-Packed Surfaces of Late Transition Metals. *Journal of Physics: Condensed Matter* **2006**, *18*, R481-R499.

18. Grånäs, E.; Andersen, M.; Arman, M. A.; Gerber, T.; Hammer, B.; Schnadt, J.; Andersen, J. N.; Michely, T.; Knudsen, J., Co Intercalation of Graphene on Ir(111) in the Millibar Regime. *The Journal of Physical Chemistry C* **2013**, *117*, 16438-16447.

19. Deng, D.; Novoselov, K. S.; Fu, Q.; Zheng, N.; Tian, Z.; Bao, X., Catalysis with Two-Dimensional Materials and Their Heterostructures. *Nature Nanotechnology* **2016**, *11*, 218-230.

20. Zeng, S.; Wang, T.; Zhang, Y.; Elmegreen, B. G.; Luan, B.; Gu, Z., Highly Efficient Co_2/C_2h_2 Separation by Porous Graphene Via Quadrupole Gating Mechanism. *Langmuir* **2023**, *39*, 8638-8645.

21. Chopra, N. G.; Luyken, R. J.; Cherrey, K.; Crespi, V. H.; Cohen, M. L.; Louie, S. G.; Zettl, A., Boron Nitride Nanotubes. *Science* **1995**, *269*, 966-967.

22. Park, H. J.; Cha, J.; Choi, M.; Kim, J. H.; Tay, R. Y.; Teo, E. H. T.; Park, N.; Hong, S.; Lee, Z., One-Dimensional Hexagonal Boron Nitride Conducting Channel. *Science Advances* **2020**, *6*, eaay4958.

23. Auwärter, W., Hexagonal Boron Nitride Monolayers on Metal Supports: Versatile Templates for Atoms, Molecules and Nanostructures. *Surface Science Reports* **2019**, *74*, 1-95.

24. Ng, M. L.; Shavorskiy, A.; Rameshan, C.; Mikkelsen, A.; Lundgren, E.; Preobrajenski, A.; Bluhm, H., Reversible Modification of the Structural and Electronic Properties of a Boron Nitride Monolayer by Co Intercalation. *ChemPhysChem* **2015**, *16*, 923-927.

25. Zhang, Y.; Weng, X.; Li, H.; Li, H.; Wei, M.; Xiao, J.; Liu, Z.; Chen, M.; Fu, Q.; Bao, X., Hexagonal Boron Nitride Cover on Pt(111): A New Route to Tune Molecule–Metal Interaction and Metal-Catalyzed Reactions. *Nano Letters* **2015**, *15*, 3616-3623.

26. Schwarz, M., et al., Corrugation in the Weakly Interacting Hexagonal-Bn/Cu(111) System: Structure Determination by Combining Noncontact Atomic Force Microscopy and X-Ray Standing Waves. *ACS Nano* **2017**, *11*, 9151-9161.

27. Dahal, A.; Batzill, M., Growth from Behind: Intercalation-Growth of Two-Dimensional Feo Moire Structure Underneath of Metal-Supported Graphene. *Scientific Reports* **2015**, *5*, 11378.

28. Naclerio, A. E.; Kidambi, P. R., A Review of Scalable Hexagonal Boron Nitride (H-Bn) Synthesis for Present and Future Applications. *Advanced Materials* **2022**, e2207374.

29. Juma, I. G.; Kim, G.; Jariwala, D.; Behura, S. K., Direct Growth of Hexagonal Boron Nitride on Non-Metallic Substrates and Its Heterostructures with Graphene. *iScience* **2021**, *24*, 103374.

30. Yang, X.; Pristovsek, M.; Nitta, S.; Liu, Y.; Honda, Y.; Koide, Y.; Kawarada, H.; Amano, H., Epitaxial Combination of Two-Dimensional Hexagonal Boron Nitride with Single-Crystalline Diamond Substrate. *ACS Applied Materials & Interfaces* **2020**, *12*, 46466-46475.

31. Li, X.; Sundaram, S.; El Gmili, Y.; Ayari, T.; Puybaret, R.; Patriarche, G.; Voss, P. L.; Salvestrini, J. P.; Ougazzaden, A., Large-Area Two-Dimensional Layered Hexagonal Boron Nitride Grown on Sapphire by Metalorganic Vapor Phase Epitaxy. *Crystal Growth & Design* **2016**, *16*, 3409-3415.

32. Wang, R., et al., A Peeling Approach for Integrated Manufacturing of Large Monolayer H-Bn Crystals. *ACS Nano* **2019**, *13*, 2114-2126.

33. Daukiya, L.; Nair, M. N.; Cranney, M.; Vonau, F.; Hajjar-Garreau, S.; Aubel, D.; Simon, L., Functionalization of 2d Materials by Intercalation. *Progress in Surface Science* **2019**, *94*, 1-20.

34. White, B.; Yin, M.; Hall, A.; Le, D.; Stolbov, S.; Rahman, T.; Turro, N.; O'Brien, S., Complete Co Oxidation over Cu_2o Nanoparticles Supported on Silica Gel. *Nano Letters* **2006**, *6*, 2095-2098.

35. Önsten, A.; Weissenrieder, J.; Stoltz, D.; Yu, S.; Göthelid, M.; Karlsson, U. O., Role of Defects in Surface Chemistry on Cu₂O(111). *The Journal of Physical Chemistry C* **2013**, *117*, 19357-19364.

36. El Kasmi, A.; Tian, Z.-Y.; Vieker, H.; Beyer, A.; Chafik, T., Innovative Cvd Synthesis of Cu₂O Catalysts for Co Oxidation. *Applied Catalysis B: Environmental* **2016**, *186*, 10-18.

37. Wu, L.-N.; Tian, Z.-Y.; Qin, W., Mechanism of Co Oxidation on Cu_2o(111) Surface: A Dft and Microkinetic Study. *International Journal of Chemical Kinetics* **2018**, *50*, 507-514.

38. Mahvash, F.; Eissa, S.; Bordjiba, T.; Tavares, A. C.; Szkopek, T.; Siaj, M., Corrosion Resistance of Monolayer Hexagonal Boron Nitride on Copper. *Scientific Reports* **2017**, *7*, 42139.

39. Li, L. H.; Xing, T.; Chen, Y.; Jones, R., Boron Nitride Nanosheets for Metal Protection. *Advanced Materials Interfaces* **2014**, *1*.

40. Scardamaglia, M.; Boix, V.; D'Acunto, G.; Struzzi, C.; Reckinger, N.; Chen, X.; Shivayogimath, A.; Booth, T.; Knudsen, J., Comparative Study of Copper Oxidation Protection with Graphene and Hexagonal Boron Nitride. *Carbon* **2021**, *171*, 610-617.

41. Kidambi, P. R.; Blume, R.; Kling, J.; Wagner, J. B.; Baehtz, C.; Weatherup, R. S.; Schloegl, R.; Bayer, B. C.; Hofmann, S., In Situ Observations During Chemical Vapor Deposition of Hexagonal Boron Nitride on Polycrystalline Copper. *Chemistry of Materials* **2014**, *26*, 6380-6392.

42. Huang, C.; Ye, W.; Liu, Q.; Qiu, X., Dispersed Cu(2)O Octahedrons on H-Bn Nanosheets for P-Nitrophenol Reduction. *ACS Applied Materials & Interfaces* **2014**, *6*, 14469-76.

43. Liang, C.; Rayabharam, A.; Aluru, N. R., Structural and Dynamical Properties of H_2o and D_2o under Confinement. *The Journal of Physical Chemistry B* **2023**, *127*, 6532-6542.

44. Auwärter, W.; Muntwiler, M.; Greber, T.; Osterwalder, J., Co on H-Bn/Ni(111): From Island to Island-Chain Formation and Co Intercalation. *Surface Science* **2002**, *511*, 379-386.

45. Yang, F.; Choi, Y.; Liu, P.; Hrbek, J.; Rodriguez, J. A., Autocatalytic Reduction of a Cu_2o/Cu(111) Surface by Co: Stm, Xps, and Dft Studies. *The Journal of Physical Chemistry C* **2010**, *114*, 17042-17050.

46. Preobrajenski, A. B.; Vinogradov, A. S.; Mårtensson, N., Ni 3d–Bn Π Hybridization at the H−Bn/Ni(111) Interface Observed with Core-Level Spectroscopies. *Physical Review B* **2004**, *70*, 165404.

47. Lee, S. H., et al., Improvements in Structural and Optical Properties of Wafer-Scale Hexagonal Boron Nitride Film by Post-Growth Annealing. *Scientific Reports* **2019**, *9*, 10590.

48. Preobrajenski, A. B.; Vinogradov, A. S.; Mårtensson, N., Monolayer of H-Bn Chemisorbed on Cu(111) and Ni(111): The Role of the Transition Metal 3d States. *Surface Science* **2005**, *582*, 21-30.

49. Gurevich, A. B.; Bent, B. E.; Teplyakov, A. V.; Chen, J. G., A Nexafs Investigation of the Formation and Decomposition of Cuo and Cu_2O Thin Films on Cu(100). *Surface Science* **1999**, *442*, L971-L976.

50. Henzler, K.; Heilemann, A.; Kneer, J.; Guttmann, P.; Jia, H.; Bartsch, E.; Lu, Y.; Palzer, S., Investigation of Reactions between Trace Gases and Functional Cuo Nanospheres and Octahedrons Using Nexafs-Txm Imaging. *Scientific Reports* **2015**, *5*, 17729.

51. Pearce, C. I.; Pattrick, R. A. D.; Vaughan, D. J.; Henderson, C. M. B.; van der Laan, G., Copper Oxidation State in Chalcopyrite: Mixed Cu D^9 and D^{10} Characteristics. *Geochimica et Cosmochimica Acta* **2006**, *70*, 4635-4642.

52. Abbate, M.; Goedkoop, J. B.; de Groot, F. M. F.; Grioni, M.; Fuggle, J. C.; Hofmann, S.; Petersen, H.; Sacchi, M., Probing Depth of Soft X-Ray Absorption Spectroscopy Measured in Total-Electron-Yield Mode. *Surface and Interface Analysis* **1992**, *18*, 65-69.

53. Hayashida, K.; Tsuda, Y.; Yamada, T.; Yoshigoe, A.; Okada, M., Revisit of Xps Studies of Supersonic O_2 Molecular Adsorption on Cu(111): Copper Oxides. *ACS Omega* **2021**, *6*, 26814-26820.

54. Gattinoni, C.; Michaelides, A., Atomistic Details of Oxide Surfaces and Surface Oxidation: The Example of Copper and Its Oxides. *Surface Science Reports* **2015**, *70*, 424-447.

55. Wiame, F.; Maurice, V.; Marcus, P., Initial Stages of Oxidation of Cu(111). *Surface Science* **2007**, *601*, 1193-1204.

56. Liu, B.-H.; Huber, M.; van Spronsen, M. A.; Salmeron, M.; Bluhm, H., Ambient Pressure X-Ray Photoelectron Spectroscopy Study of Room-Temperature Oxygen Adsorption on Cu(100) and Cu(111). *Applied Surface Science* **2022**, *583*, 152438.

57. Singh, B.; Mehta, B. R., Relationship between Nature of Metal-Oxide Contacts and Resistive Switching Properties of Copper Oxide Thin Film Based Devices. *Thin Solid Films* **2014**, *569*, 35-43.

58. Nagashima, A.; Tejima, N.; Gamou, Y.; Kawai, T.; Oshima, C., Electronic Structure of Monolayer Hexagonal Boron Nitride Physisorbed on Metal Surfaces. *Physical Review Letters* **1995**, *75*, 3918-3921.

59. Therrien, A. J.; Zhang, R.; Lucci, F. R.; Marcinkowski, M. D.; Hensley, A.; McEwen, J.-S.; Sykes, E. C. H., Structurally Accurate Model for the "29"-Structure of Cu_XO/Cu(111): A Dft and Stm Study. *The Journal of Physical Chemistry C* **2016**, *120*, 10879-10886.

60. Gloystein, A.; Nilius, N.; Goniakowski, J.; Noguera, C., Nanopyramidal Reconstruction of Cu_2O(111): A Long-Standing Surface Puzzle Solved by Stm and Dft. *The Journal of Physical Chemistry C* **2020**, *124*, 26937-26943.

61. Soon, A.; Todorova, M.; Delley, B.; Stampfl, C., Oxygen Adsorption and Stability of Surface Oxides on Cu(111): A First-Principles Investigation. *Physical Review B* **2006**, *73*, 165424.

62. Hensley, A. J. R.; Therrien, A. J.; Zhang, R.; Marcinkowski, M. D.; Lucci, F. R.; Sykes, E. C. H.; McEwen, J.-S., Co Adsorption on the "29" Cu_xo/Cu(111) Surface: An Integrated Dft, Stm, and Tpd Study. *The Journal of Physical Chemistry C* **2016**, *120*, 25387-25394.

63. Beckord, J.; Diulus, J. T.; Novotny, Z.; Osterwalder, J.; Hengsberger, M., Protected Ultrathin Cuprous Oxide Film for Photocatalysis: Excitation and Relaxation Dynamics. *Physical Review Materials* **2023**, *7*, 045801.

64. Matencio, S.; Barrena, E.; Ocal, C., Coming across a Novel Copper Oxide 2d Framework During the Oxidation of Cu(111). *Physical Chemistry Chemical Physics* **2016**, *18*, 33303-33309.

65. Jenkins, L. H.; Chung, M. F., Leed and Auger Investigations of Cu (111) Surface. *Surface Science* **1971**, *24*, 125-139.

66. Roth, S.; Matsui, F.; Greber, T.; Osterwalder, J., Chemical Vapor Deposition and Characterization of Aligned and Incommensurate Graphene/Hexagonal Boron Nitride Heterostack on Cu(111). *Nano Letters* **2013**, *13*, 2668-75.

67. Novotny, Z., et al., Probing the Solid–Liquid Interface with Tender X Rays: A New Ambient-Pressure X-Ray Photoelectron Spectroscopy Endstation at the Swiss Light Source. *Review of Scientific Instruments* **2020**, *91*, 023103.

68. Comini, N.; Huthwelker, T.; Diulus, J. T.; Osterwalder, J.; Novotny, Z., Factors Influencing Surface Carbon Contamination in Ambient-Pressure X-Ray Photoelectron Spectroscopy Experiments. *Journal of Vacuum Science & Technology A: Vacuum, Surfaces, and Films* **2021**, *39*, 043203.

69. Judd, R. W.; Hollins, P.; Pritchard, J., The Interaction of Oxygen with Cu(111): Adsorption, Incorporation and Reconstruction. *Surface Science* **1986**, *171*, 643-653.

70. Baber, A. E., et al., *In Situ* Imaging of Cu_2o under Reducing Conditions: Formation of Metallic Fronts by Mass Transfer. *Journal of the American Chemical Society* **2013**, *135*, 16781-16784.

71. Raabe, J., et al., Pollux: A New Facility for Soft X-Ray Spectromicroscopy at the Swiss Light Source. *Review of Scientific Instruments* **2008**, *79*, 113704.

72. Fadley, C., *Basic Concepts of X-Ray Photoelectron Spectroscopy*; Academic Press: London, England, UK, 1978; Vol. 2, p 1-156.

73. Muntwiler, M., et al., Surface Science at the Pearl Beamline of the Swiss Light Source. *Journal of Synchrotron Radiation* **2017**, *24*, 354-366.

74. Choi, J. I. J.; Mayr-Schmölzer, W.; Mittendorfer, F.; Redinger, J.; Diebold, U.; Schmid, M., The Growth of Ultra-Thin Zirconia Films on $Pd_3Zr(0001)$. *Journal of Physics: Condensed Matter* **2014**, *26*, 225003.

75. Greif, M.; Castiglioni, L.; Becker-Koch, D.; Osterwalder, J.; Hengsberger, M., Acquisition of Photoelectron Diffraction Patterns with a Two-Dimensional Wide-Angle Electron Analyzer. *Journal of Electron Spectroscopy and Related Phenomena* **2014**, *197*, 30-36.

76. Jensen, F.; Besenbacher, F.; Legsgaard, E.; Stensgaard, I., Oxidation of Cu(111): Two New Oxygen Induced Reconstructions. *Surface Science Letters* **1991**, *259*, L774-L780.

77. García de Abajo, F. J., Electron Diffraction in Atomic Clusters (Edac) for the Simulation of Photoelectron Diffraction (Pd). http://widgets.nanophotonics.es/edac/manual/edac.html **1999**.

78. García de Abajo, F. J.; Van Hove, M. A.; Fadley, C. S., Multiple Scattering of Electrons in Solids and Molecules: A Cluster-Model Approach. *Physical Review B* **2001**, *63*, 075404.

79. Seah, M. P.; Dench, W. A., Quantitative Electron Spectroscopy of Surfaces: A Standard Data Base for Electron Inelastic Mean Free Paths in Solids. *Surface and Interface Analysis* **1979**, *1*, 2-11.

80. Kühne, T. D., et al., Cp2k: An Electronic Structure and Molecular Dynamics Software Package - Quickstep: Efficient and Accurate Electronic Structure Calculations. *The Journal of Chemical Physics* **2020**, *152*, 194103.

81. Goedecker, S.; Teter, M.; Hutter, J., Separable Dual-Space Gaussian Pseudopotentials. *Physical Review B* **1996**, *54*, 1703-1710.

82. VandeVondele, J.; Hutter, J., Gaussian Basis Sets for Accurate Calculations on Molecular Systems in Gas and Condensed Phases. *The Journal of Chemical Physics* **2007**, *127*, 114105.

83. Bengtsson, L., Dipole Correction for Surface Supercell Calculations. *Physical Review B* **1999**, *59*, 12301-12304.

84. Perdew, J. P.; Burke, K.; Ernzerhof, M., Generalized Gradient Approximation Made Simple. *Physical Review Letters* **1996**, *77*, 3865-3868.

85. Grimme, S., Semiempirical Gga-Type Density Functional Constructed with a Long-Range Dispersion Correction. *Journal of Computational Chemistry* **2006**, *27*, 1787-1799.

86. Byrd, R. H.; Lu, P.; Nocedal, J.; Zhu, C., A Limited Memory Algorithm for Bound Constrained Optimization. *SIAM Journal on Scientific Computing* **1995**, *16*, 1190-1208.

87. Tersoff, J.; Hamann, D. R., Theory of the Scanning Tunneling Microscope. *Physical Review B* **1985**, *31*, 805-813.

88. Iannuzzi, M.; Hutter, J., Inner-Shell Spectroscopy by the Gaussian and Augmented Plane Wave Method. *Physical Chemistry Chemical Physics* **2007**, *9*, 1599-1610.

89. Slater, J. C.; Johnson, K. H., Self-Consistent-Field *Xα* Cluster Method for Polyatomic Molecules and Solids. *Physical Review B* **1972**, *5*, 844-853.

90. Jensen, F.; Besenbacher, F.; Stensgaard, I., Two New Oxygen Induced Reconstructions on Cu(Lll). *Surface Science* **1992**, *269/270*, 400-404.

91. Yang, F.; Choi, Y.; Liu, P.; Stacchiola, D.; Hrbek, J.; Rodriguez, J. A., Identification of 5-7 Defects in a Copper Oxide Surface. *Journal of the American Chemical Society* **2011**, *133*, 11474-7.

92. Axnanda, S.; Scheele, M.; Crumlin, E.; Mao, B.; Chang, R.; Rani, S.; Faiz, M.; Wang, S.; Alivisatos, A. P.; Liu, Z., Direct Work Function Measurement by Gas Phase Photoelectron Spectroscopy and Its Application on Pbs Nanoparticles. *Nano Letters* **2013**, *13*, 6176-82.

93. Grad, L.; Novotny, Z.; Hengsberger, M.; Osterwalder, J., Influence of Surface Defect Density on the Ultrafast Hot Carrier Relaxation and Transport in Cu_2O Photoelectrodes. *Scientific Reports* **2020**, *10*, 10686.

94. Diulus, J. T., et al., Ambient-Pressure X-Ray Photoelectron Spectroscopy Characterization of Radiation-Induced Chemistries of Organotin Clusters. *ACS Applied Materials & Interfaces* **2019**, *11*, 2526-2534.

95. Diulus, J. T.; Frederick, R. T.; Hutchison, D. C.; Lyubinetsky, I.; Addou, R.; Nyman, M.; Herman, G. S., Effect of Ambient Conditions on Radiation-Induced Chemistries of a Nanocluster Organotin Photoresist for Next-Generation Euv Nanolithography. *ACS Applied Nano Materials* **2020**, *3*, 2266-2277.

96. Spitzer, A.; Luth, H., The Adsorption of Oxygen on Copper Surfaces Ii. Cu(111). *Surface Science* **1982**, *118*, 136-144.

97. Piccinin, S., et al., Alloy Catalyst in a Reactive Environment: The Example of Ag-Cu Particles for Ethylene Epoxidation. *Physical Review Letters* **2010**, *104*, 035503.

98. Wolfgang, W.; Werner, S.; Cedric, P.; Justin, G., Simulation of Electron Spectra for Surface Analysis (Sessa)Version 2.2 User's Guide. *Natl Std. Ref. Data Series (NIST NSRDS),* National Institute of Standards and Technology **2021**, Gaithersburg, MD.

99. Joshi, S., et al., Boron Nitride on Cu(111): An Electronically Corrugated Monolayer. *Nano Letters* **2012**, *12*, 5821-8.

ASSOCIATED CONTENT

Data And Materials Availability

The data both presented and not presented in this report, which support the findings of this study, are available on Zenodo.org at the following doi: 10.5281/zenodo.7448521

Supplementary Materials

The Supporting Information document contains further preparation and characterization results from experiments mentioned in the text and additional experiments for supporting arguments. The contents of the document are as follows:

Materials and Methods

Supplementary Text

(1) Initial Intercalation Studies

(2) Preparation of a well-ordered Oxide

Figs. S1 to S19

References (64–99)

AUTHOR INFORMATION

Corresponding Author

*****Corresponding author. Email: trey.diulus@psi.ch

Present Addresses

†Current address: Physical and Computational Sciences Directorate and Institute for Integrated Catalysis, Pacific Northwest National Laboratory, Richland, Washington 99352, United States

Author Contributions

The manuscript was written through contributions of all authors. All authors have given approval to the final version of the manuscript.

Conceptualization: JTD, ZN, ND, MH, MI, JO

Methodology: JTD, ZN, ND, YA, NC, JB, MM, MH, MI, JO

Investigation: JTD, ZN, YA, ND, NC, JB

Visualization: ZN, JO

Funding acquisition: JTD, JO

Project administration: JO

Supervision: MI, ZN, JO

Writing – original draft: JTD, ZN, ND

Writing – review & editing: ZN, MH, MI, JO

Funding Sources

Swiss National Science Foundation through grant numbers 200020_172641 and 200020_200303, and also through the National Center of Competence in Research (NCCR) Molecular Ultrafast Science and Technology (MUST)

European Union's Horizon 2020 program (FP-RESOMUS - MSCA 801459)

ACKNOWLEDGMENTS

This work was performed at both the In Situ Spectroscopy (X07DB) and the PEARL (X03DA) beamlines of the Swiss Light Source, at the Paul Scherrer Institut, in Villigen PSI, Switzerland, using the Solid Liquid Interface Chamber (SLIC) and PEARL endstations. We would like to acknowledge Blagoj Sarafimov for his repeated help with equipment preparation and endstation development. We also acknowledge the support at the ISS beamline provided by Dr. Luca Artiglia and Dr. Jörg Raabe, as well as Patrick Ascher from the PEARL beamline. We gratefully acknowledge computational support from the Swiss National Supercomputing Centre (CSCS) under the projects s965 "Molecules at interfaces from density functional theory'', s1198 "Catalysis under cover: the case of the hybrid h-BN/Cu_2O/Cu heterostructure", and uzh35 as financed through the support of the Alfred Werner Legat.

Supplementary Materials for

h-BN/metal-oxide interface grown by intercalation: A model system for nano-confined catalysis

J. Trey Diulus,[1,2*] Zbynek Novotny,[1,2†] Nanchen Dongfang,[3] Jan Beckord,[1] Yasmine Al-Hamdani,[3,4] Nicoló Comini,[1,2] Matthias Muntwiler,[2] Matthias Hengsberger,[1] Marcella Iannuzzi,[3] Jürg Osterwalder[1]

[1]Department of Physics, University of Zürich, Irchel Campus; 8057 Zürich, Switzerland

[2]Swiss Light Source, Paul Scherrer Institute; 5232 Villigen PSI, Switzerland

[3]Department of Chemistry, University of Zürich, Irchel Campus; 8057 Zürich, Switzerland

[4]Department of Earth Sciences, University College London, London WC1E 6BT, United Kingdom

*Corresponding author. Email: trey.diulus@psi.ch

This PDF file includes:

MATERIALS AND METHODS

A Cu(111) single crystal (purity 6N, miscut accuracy ~0.1°, polished to a roughness $R_a < 0.03$ μm) was purchased from Surface Preparation Laboratory B.V. (Netherlands). A SPECS cold-cathode Penning ion source (discharge voltage 500V, accelerating voltage 500 V, ion current I_{Ar+} ~0.7 μA/cm^2) was used for ion sputtering, typically for ~30 min, followed by UHV (<10^{-9} mbar) annealing to ~800 °C with a e-beam heater (Ferrovac, 45 mA emission, ~45 W). Several Ar^+ sputtering and annealing cycles were performed to obtain a clean and ordered surface verified by LEED and AES.

A single layer of h-BN was deposited on Cu(111) *via* chemical vapor deposition (CVD) by exposing the sample to borazine at a pressure of 2-3×10^{-6} mbar, while the sample temperature was nominally 800 °C (+/- 20 °C), based on calibration of the e-beam annealing stage with a type K thermocouple. The purity of the borazine was verified before dosing using quadrupole mass spectrometry (QMS). The sample was exposed for 10 to 15 minutes (depending on the pressure setpoint) resulting in ~2000 L dose, consistent with prior recipes for monolayer h-BN deposition on Cu(111).[23]

The h-BN layer is characterized in the same area with both low-energy electron diffraction (LEED) and Auger electron spectroscopy (AES), displayed in figure S1. The clean Cu(111) surface in figure S1c shows six sharp diffraction spots in a hexagon pattern, consistent with the reciprocal lattice of Cu(111).[64] The AES spectrum plotted in blue in figure S1d shows no contamination other than adventitious carbon and Ar implanted during ion sputtering.[65] A LEED image taken after the deposition of h-BN is shown in figure S1b, where a faint background intensity is seen in the close vicinity of the Cu(111) diffraction spots, mainly along the radial direction.[66] This is due to the lattice mismatch between the h-BN layer and the Cu(111)

surface where the background intensity results from a slight difference in the in-plane reciprocal lattice vectors of h-BN and Cu.[66] The AES spectrum of h-BN/Cu(111) is plotted in black in figure S1d, where a distinct change in seen in the 100-200 eV range as the peaks resulting from Cu MNN signal are overlapped with B KLL peaks. The N KLL peaks are also present following h-BN deposition.

Oxidation of h-BN/Cu(111) took place in the analysis chamber (AC) of the solid-liquid interface chamber (SLIC),[67] which was backfilled with up to p_{O2} = 1 mbar at 200 °C using Minican® bottles (Pangas, 5N). The pressure was measured with a combined Pirani/capacitance gauge (Pfeiffer PCR 280) to cover the pressure range needed for ambient-pressure experiments (5×10^{-4} mbar to 1000 mbar). Once the pressure was stabilized, time-lapsed XPS were collected until a sufficient signal-to-noise ratio was achieved. The AC chamber was then pumped and returned to high vacuum (HV, ~1×10^{-7} mbar) for taking XPS spectra after O_2 exposure.

Following the initial APXPS measurements of the thermal stability, oxidation of a well-ordered h-BN/Cu(111) interface was prepared using ~5-40 min oxygen exposure without exposure to the X-ray beam to avoid buildup of carbon contamination or enhanced oxidation due to excited oxygen.[68] Moreover, the sample was moved sufficiently (~10 mm) far away from the analyzer cone and rotated in the opposite direction to avoid variation of temperature and pressure across the sample surface. After oxidation, the O KLL peaks appear in the AES spectrum plotted in green in figure S1d. Faint extra diffraction spots add a noticeable increase in background intensity in the center of figure S1a. By decreasing the e-beam current and lowering the energy to 40 eV, we can more clearly see the diffraction spots corresponding to the reciprocal oxide lattice, shown in figure S2. The spots form a hexagon shape, which corresponds well with the FFT of the STM image presented in Figure 1 and further described in figure S3. The LEED spots shown in figure S2 are also shown alongside simulated diffraction spots using the LEEDLab

2018 V1.2 software package. The length×width of the cell representing the simulated spots in green is 10.2 × 10.2 Å^2 with an angle of 60°, corresponding to an epitaxial matrix of $\begin{vmatrix} 4 & 0 \\ 0 & 4 \end{vmatrix}$ and providing an almost perfect match to the measured spots. A simulated real space coverage is also shown in figure S2 corresponding to the periodicity of the chemisorbed oxide.

When changing the electron energy to higher values (>100 eV), a LEED pattern remarkably similar to the $\begin{vmatrix} 3 & 2 \\ -1 & 2 \end{vmatrix}$ overlayer with three rotational domains reported in Judd et al. can be seen,[69] but the lack of spots seen at 40 eV suggest that we have a base periodicity that is likely destroyed and prefers a larger unit cell seen by LEED. Significant literature has studied Cu surface oxidation, where STM of the "29" and "44" strongly resembles the stripe feature we see in our measured STM for a constrained Cu_2O lattice on top of a Cu(111) substrate,[70] therefore we modeled the hexagonal structure similarly albeit the "29" and "44" unit cells are significantly larger. In our case, the h-BN lattice above the Cu_2O will also influence the size of the unit cell.

APXPS measurements were carried out at the Solid-Liquid Interface Chamber (SLIC) endstation[67] to obtain a temperature and pressure dependence for O_2 intercalation through h-BN. The SLIC utilizes a Scienta R4000 HiPP-2 ambient pressure electron analyzer that is attached to the In Situ Spectroscopy (ISS) beamline (X07DB) that is nearly identical as the beamline X07DA described by Raabe et al..[67, 71] The beamline uses a double crystal monochromator with a 300-400 μm spot size and an average beam current of 17 μA measured with a photodiode (AXUV100) at a photon energy of 1000 eV.[67, 71]

Fast XPS spectra were acquired using a photon energy (*hv*) of 700 eV at an emission angle of 30° with linearly polarized light, where the polarization vector was aligned with the optical path of the electron spectrometer. The sample was irradiated at 60° with respect to the surface normal. Photoelectrons were detected using a pass energy of 20 eV with a fully open

analyzer slit. The binding energy scale was calibrated using the Au 4f core level peak position on a polycrystalline gold sample with a resolution of 0.77 eV relating to the full-width half maximum (FWHM) of Au 4f collected with the same beam energy and analyzer settings as used for all experiments. XPS measurements for an ordered oxide used a different lens mode with a 50 eV pass energy for an increased signal-to-noise ratio without significantly sacrificing the resolution. A slightly higher photon energy of 720 eV was also used to avoid overlap of the O KLL with the B 1s peak. The heating was performed using a pyrolytic boron nitride heater in direct contact with the sample holder, and the temperature was measured with a Pt100 sensor placed in close proximity to the sample holder. Prior to all data collection, the analysis chamber was flushed with 2 mbar of oxygen and the heater was outgassed to a temperature of 250 °C. No contamination was detected other than adventitious carbon. All XPS spectra were processed using IgorPRO (Wavemetrics Inc.) and CasaXPS software packages, and any quantitative measurements were calculated using the Fadley method for polarized light parallel to the emission vector.[72]

Further characterization of the h-BN/$Cu_{2-x}O$/Cu(111) sample was carried out at the PEARL endstation.[73] Sample preparation of h-BN/$Cu_{2-x}O$/Cu(111) was performed in the SLIC endstation,[67] prior to beamtime at the PEARL endstation. Preparation of h-BN/Cu(111) was still done identically, as mentioned above. Oxidation of the Cu(111) substrate underneath the h-BN cover *via* O_2 intercalation was performed by exposure to p_{O2} = 1 mbar at 150 °C for 5-40 min in the SLIC analysis chamber.[67] LEED and AES were collected to ensure an ordered oxide structure was formed, and the h-BN monolayer remained intact in agreement with previous experiments. Samples were then transferred to PEARL from the SLIC endstation using a custom-built vacuum suitcase equipped with a sorption pump, capable of holding the pressure in the suitcase to $<8\times10^{-9}$ mbar. While the vacuum suitcase should hold the pressure well, the sample

still needs to be transferred through the loading chamber at PEARL after being vented to attach the suitcase, providing approximately a 10 min exposure to 10^{-6} mbar vacuum.

All experiments at the PEARL endstation took place at a base pressure below 2×10^{-10} mbar.[73] Topographical images of the sample were obtained using a low-temperature STM (Omicron Nanotechnology GmbH) at 78 K using a constant current mode and etched tungsten and PtIr tips.[73] STM image processing and analysis were performed in the ImageJ software package using custom-made plugins described in Choi et al..[74] The PEARL endstation utilizes a Scienta EW4000 hemispherical electron analyzer with two-dimensional detection attached to the PEARL beamline (X03DA).[73] The beamline uses a plane grating monochromator with a 170×70 μm^2 spot size and an average photon flux of 2×10^{11} ph/s measured with a photon energy of 1000 eV.[73] The beamline has a resolution of 0.85 eV and 0.7 eV for 1500 and 720 eV photon excitation energies, respectively, calibrated to the FWHM of Au $4f_{7/2}$. A reference current is measured using a Pt mirror, allowing for the collection of a current profile that can be used for normalizing XAS TEY spectra. An additional XAS reference was collected using a freshly Ar^+ sputtered polycrystalline Cu to avoid normalization with spectra of oxygen contamination on the Pt mirror of the beamline optics.

The PEARL sample manipulator is designed for angle-resolved XPS collection, with a polar rotation (θ) from 0° to 180°, a tilt rotation (ψ) from -28° to +28°, an azimuthal rotation (φ) of -180° to 180°, and achieving an angle resolution of 0.5°.[73] Photoelectron spectra can be collected with respect to all three angles, allowing for collection of a full hemispherical diffractogram.[73] The 2D detector is additionally capable of collecting spectra from a photoemission angle (α) of -25° to +25° in parallel. The diffractogram contains a distribution of spectra for the range of α corresponding to a θ and ψ for each scan collected. The spectra can then be fitted to determine the signal intensity with respect to angle and then plotted to form an

XPD pattern. All XPD patterns, both from experimental and simulated data, were plotted in IgorPRO using custom made macros. The algorithms behind these plugins are extensively described by Greif et al..[75] These data were then exported into ImageJ where a Gaussian blur with a reduced standard deviation (σ_r) of 5.0 was used to interpolate the diffractogram.

An initial model of h-BN on Cu(111) shown in figure S18 was generated using a Python script that calculated the atomic coordinates within a large cluster for Cu(111) and h-BN, and then exported these values into a text file that could be open with the VESTA software. A Van der Waals gap of 3 Å was integrated into the model manually. The oxidized cluster shown in figure S19 was generated using first the model from figure S18 and manually integrating one layer of a Cu_2O lattice,[76] of which only a trilayer was used. In order to make the lattice of the Cu_2O match, the dimensions of the unit cell were decreased from 3.49×6.04 Å reported in Jensen et al.[76] to 3.37×5.9 Å, and then allowed to relax. To establish an energetically favorable heterostructure that is consistent with the experimental information available, we considered several adsorption sites for chemisorbed O atoms on the Cu(111) surface and below the $Cu_{2-x}O$ layer: Cu_{top}, Cu_{hcp}, Cu_{fcc}. By relaxing the atomic positions with DFT, we find that O atoms are not stable on Cu_{top} sites and relax to nearby Cu_{hcp} and Cu_{fcc} sites. Comparing the binding energy of chemisorbed O atoms at Cu_{hcp} (1.35 eV) and Cu_{fcc} (1.45 eV) sites, we find that the Cu_{fcc} site is 0.10 eV more stable than the Cu_{hcp} site, per chemisorbed O atom. Thus, the h-BN/$Cu_{2-x}O$/Cu(111) with chemisorbed O atoms at Cu_{fcc} sites is used for further characterization of the heterostructure and comparison with experiment. This model, shown in Figure 2 and figure S19, was used for all simulated data of the h-BN/$Cu_{2-x}O$/Cu(111) heterostructure presented in this paper.

EDAC input files[77-78] were generated following the user guide each with the geometry, polarization, and kinetic energy of the excited electrons relative to what is expected from the

PEARL endstation, along with the inelastic mean free paths described by the Seah, Dench Universal Curve (SD-UC).[79] Emitters were chosen from a centralized unit cell that was surrounded by additional unit cells of which the same atoms were not chosen as emitters, thus removing edge effects from the simulation. Scattering potentials were calculated using the Muffin Tin model. The maximum hopping distance (d_{max}) was set to 15 Å and the energy of the vacuum level was set to 15 eV relative to the Muffin Tin zero. The maximum effective angular momentum (l_{max}) was set to 15 and up to 10 orders of iteration were set for an emission angle window of 1°. All simulated data were additionally processed using custom-made macros from IgorPRO.

All DFT calculations were performed using the Quickstep module of the CP2K version 10.0 (Development version) program package.[80] For geometrical optimization and electronic structure calculations, the Kohn-Sham DFT within the hybrid Gaussian and plane waves framework (GPW) was applied, with Goedecker-Teter-Hutter (GTH) pseudopotentials.[81] The molecular orbitals of the valence electrons are expanded in molecularly optimized (MOLOPT) Gaussian basis sets.[82] More specifically, DZVP-MOLOPT-GTH primary basis sets have been used for all atoms. For the auxiliary plane waves basis set a cutoff of 600 Ry has been applied. All calculations are done within periodic boundary conditions, use Gamma point only and are spin-polarized. Since we used an asymmetric slab model, where the heterostructure is constructed only on one side, the surface dipole correction has been always applied along the z-axis.[83] Structural and electronic properties are computed at the GGA level of theory, using the Perdew-Burke-Ernzerhof (PBE) functional,[84] augmented by the Grimme-D3 scheme to correct for the missing dispersion contributions.[85] The geometry optimization applies the Broyden-Fletcher-Goldfarb-Shanno (BFGS) scheme,[86] with a force threshold of 10^{-3} Hartree /Bohr. The h-BN/$Cu_{2-x}O$/Cu(111) with chemisorbed O atoms heterostructure consists of a four layer thick

(4×4) Cu(111) slab, surmounted on one side by one tri-layer Cu_2O(111)-V(CUS)-(1×1) (where all unsaturated Cu atoms have been removed) plus four chemisorbed oxygen atoms (placed either at Cu(111) fcc, hcp, or top sites) and an (8×8) h-BN monolayer. The lateral dimensions of the simulation cell are 20.5×17.7 $Å^2$. Sufficient vacuum space (20 Å) above the oxide/h-BN interface prevents spurious physical interactions among the periodic images.

Projected densities of states are obtained by projecting the electronic density contributions onto the atomic orbitals of the basis set. The computed STM image was obtained using the Tersoff−Hamann simulations.[87] The calculation of the N, B, and O K-edges to reproduce the XAS data has been achieved by applying the Gaussian augmented plane wave method under the half-core hole approximation,[88] where for the light elements all electrons are explicitly considered (no pseudopotentials) and 6-311G** all-electron basis sets were employed to expand the molecular orbitals. The calculations of the XAS spectra are based on the half-core hole approximation, where initial and final state effects are accounted for by electronic energy eigenvalue calculations after removing half an electron from the core state.[89] We performed a delta SCF calculation to get an accurate energy for the first transition, and rigidly shift the absorption spectrum.

SUPPLEMENTARY TEXT

(1) Initial Intercalation Studies

To evaluate the pressure dependence of the oxide formation *via* intercalation that occurs during exposure of h-BN/Cu(111) to O_2 *in-situ,* we utilize APXPS, where data were collected during and following exposure to p_{O2} = 0.001, 0.05, and 1 mbar for ~2 hours at each pressure, all

at room temperature (RT). We collected high-resolution core-level spectra for O 1s, Cu 3p, N 1s, C 1s, and the valence level for each pressure with hν = 700 eV photon excitation energy. B 1s spectra were collected only before and after exposure due to the increase in the intensity of the O KLL Auger peak that overlaps with the B 1s peak at this photon energy. Therefore, later experiments were collected using hν = 720 eV photon excitation energy to avoid any Auger background for all core-level peaks of interest.

In figure S4, a comparison of spectra for each pressure condition is shown described for the O 1s, N 1s, Cu 3p, and C 1s. The O 1s spectra (figure S4a) show the biggest change, starting from only weak adventitious species seen before oxidation (purple) with a peak at 531.7 eV. After p_{O2} = 0.001 mbar exposure, two peaks form at 529.1 and 530.4 eV. These energies typically correspond to chemisorbed O (blue)[56] and $Cu_{2-x}O$ pyramids or clusters (green),[60] respectively. More detail on these peaks is provided below and in the main text in the context of higher resolution XPS data collected at UHV. For the current description, these metal oxide peaks are two of three peaks known to be the primary fingerprints for the oxidation of the Cu(111) substrate. The third peak is the hexagonal surface oxide at 529.5 eV. As the pressure increases from 0.001 to 0.05 mbar exposure, the cluster peak (green) increases, and the chemisorbed oxide (blue) is no longer present. Instead, a small presence of the hexagonal structure is seen, but this low intensity is expected as temperature is needed to form a homogeneous and ordered structure. Several groups studying well-ordered hexagonal $Cu_{2-x}O$ surface oxides report annealing temperatures of at least 100 °C or greater either during[59, 90-91] or after exposure to O_2.[69, 90-91] Since the hexagonal surface oxide peak remains relatively the same intensity after increasing to 1 mbar, the surface is now saturated and more island clusters coalesce as oxygen diffuses into the substrate, following the mechanism suggested by Gloystein et al..[60] This also resembles the mechanism supported by combined STM and DFT experiments

by calculating a phase diagram with the O chemical potential.[59] Liu et al. have additionally seen the same behavior, where a Cu_2O peak at 530.4 eV increases with increasing O_2 exposure for room temperature APXPS measurements on Cu(111) without h-BN present.[56]

Two additional peaks in the O 1s spectra at higher binding energy are assigned to adventitious contamination. They are more pronounced already following exposure to p_{O2} = 0.001 mbar. Unfortunately, due to the presence of the focused synchrotron beam during oxidation combined with the high pressure backfilled in the chamber, a significant amount of oxidation to hydrocarbon contaminants takes place on the surface,[68] which considerably drowns the signal intensity of the oxide and h-BN layer. The peak at 531.6 eV corresponds to oxygen bound to carbon (O-C) and a final peak at 533 eV represents hydroxyl (O-H) bonds on the surface. The intensities of these two contamination peaks (O-C and O-H) increase with increasing pressure, as beam-induced carbon buildup is common for synchrotron based APXPS measurements,[68] while additionally the chamber is not baked and has a base pressure of only $\sim 5\times10^{-9}$ mbar due to a sample loading door that uses a Viton™ O-ring. Moreover, there is residual water vapor from liquid-based experiments done previously in this chamber.[67] When high pressures are introduced into the chamber, water on the chamber walls can be displaced and contaminate the surface. Thus, to reduce the signal consumption of continuous contamination buildup, numerous spots were collected successively, in which a "fresh" spot was chosen for each change in pressure or temperature conditions.

B 1s data is not shown from this dataset due to an increasing peak corresponding to O KLL that overlaps with the primary B 1s peak. No visible change is seen between the Cu 3p spectra, where the Cu 3p doublet remains with the same FWHM, spin-orbit branching ratio, and energy positions at 75 and 77.4 eV, respectively. The N 1s initially has a sharp Gaussian peak at 397.8 eV for the N-B bond of the h-BN, as well as a shoulder peak at 398.4 eV representing

defects in the h-BN lattice.[26] The C 1s baseline spectrum shows the adventitious C-C/C-H peak at 284.6 eV (blue), with a significant increase once exposed to 0.001 mbar of O_2. An increase in oxidized carbon species is seen with peaks at 285.9 eV (C-O, red), 287 eV (C=O, green), and 288.2 eV (O-C=O, purple) most likely due to irradiation during oxygen exposure. The value of oxidized carbon and overall carbon intensity varies when moving to a "fresh" spot that was not irradiated but exposed to the same ambient conditions.[68]

Due to the excessive build-up of carbon and water at room temperature, along with the length of time to obtain intercalated oxidation, the experiment was repeated by using a constant pressure and increasing the temperature while collecting spectra simultaneously. In figure S5, heat maps of APXPS spectra are shown versus sequential iterations for N 1s and O 1s for the oxidation of the Cu(111) underneath h-BN by exposure to p_{O2} = 1 mbar while annealing up to 200 °C with 50 °C steps. These heat maps provide a temperature dependence for intercalation and Cu(111) oxidation, while also determining the limit for the stability of the h-BN cover in an O_2 ambient. During each iteration, six core levels (O 1s, C 1s, B 1s, N 1s, Cu 3p, and the valence level) were collected sequentially corresponding to a total of 2.3 min between each sequence of scans. The two most important spectra are the N 1s and O 1s, shown in figure S5a and b, along with a temperature profile with respect to time and iteration shown in figure S5c. Initially, as the temperature remains 100 °C or below, an N 1s peak corresponding to the h-BN monolayer is seen at 398 eV, roughly up until iteration 200 (~ 7.7 hours). For this same initial timeframe, the O 1s displays a doublet at 539.0/540 eV attributed to gas phase oxygen. Towards the end of the 150 °C sequences (approximately 1.9 hours of exposure at 150 °C as the temperature begins ramping to 200 °C), a noticeable peak emerges in the O 1s at 530 eV signifying substantial oxidation of the Cu(111) substrate. A shift in the gas phase O peak down to 538.0/539.0 eV also suggests an increase in the work function of the sample,[92] also seen in high-resolution spectra

discussed later in the supplemental text. At this point, the N 1s also is no longer detectable, as the h-BN layer is destroyed.

The sample initially had a color typical for metallic copper, shown in figure S5d, with a white ring on the perimeter present due to the reflection of the viewport when taking the picture. A considerable change occurred visually on the sample, changing color to a more reddish-orange surface seen in figure S5e and no longer reflective. A plume-like shape is also seen on the surface, with a green outer ring, where green is generally attributed to copper hydroxide, although this could also be due to Newton rings from a variable oxide thickness. This plume and variable oxidation are due to the sample being very close to the analyzer cone, providing a temperature and pressure gradient across the surface, while simultaneously being exposed to the x-ray beam. The plume shape and a significant carbon uptake do not occur with later oxidation experiments done with the sample far away from the cone and no concurrent irradiation.

Following the thermal stability experiment, the sample was repaired through numerous (25+) sputter-anneal cycles, in addition to several (4-5) 30 min annealing treatments in 1×10^{-6} mbar partial pressure of H_2. Annealing in the presence of reducing agents was required to quickly remove oxygen from the surface with each cycle. Annealing in borazine was also effective, but the reaction would lead to residual B on the surface, therefore H_2 was used until the sample was repaired and then h-BN was grown afterwards. Once the Cu(111) sample was restored, a layer of h-BN was deposited (verified by LEED and AES), and the oxidation experiment was repeated using a maximum temperature of 150 °C. A CCD camera was used to track any visible changes in the surface throughout the oxidation process, which allowed for the ability to immediately purge the chamber and cool the sample if a change in reflectivity on the surface was noticed, shown in Figure S6.

To explore the parameter space for the optimal growth of ordered Cu_2O *via* oxygen intercalation, APXPS data were collected for various temperatures and pressures where both were utilized as a constant or as a variable. At each temperature and pressure interval, a dataset was collected comprising each core-level region mentioned above, along with XAS. The time for one typical dataset collection is approximately 2 hours. Initially, the sample was exposed to 1 mbar O_2 partial pressure at RT for the duration of a dataset collection, followed by pumping back to HV and then stepwise annealing to 100 °C, collecting a dataset at 50, 75, and 100 °C during the anneal. XPS spectra were then collected after returning directly to RT following the anneal. No significant changes different from what was already presented for RT exposures were observed.

Afterwards, the sample was exposed to 1 mbar O_2 while simultaneously annealing to 100 °C and collecting XPS data at elevated temperature and pressure. Once a full dataset was collected, the temperature and pressure were once again returned to RT and HV, respectively, for the collection of another dataset. This additionally yielded the same result at RT measurements, albeit with less overall carbon, yet no change was seen in the O 1s that would suggest an ordered intercalated oxide. The sample was then annealed to a higher temperature of 150 °C while being simultaneously exposed to 1 mbar O_2. Midway through the dataset collection during this experiment, a slight change in the optical appearance of the sample was noticed on the CCD camera and the system was pumped immediately to $<1\times10^{-6}$ mbar after ~70 min of oxidation time, followed by XPS collection during the cooldown and at RT. The highlights of this change in the surface optical properties are shown in figure S6.

Following the temperature dependence experiment, we see in figure S7 specifically after **1)** annealing to 100 °C in UHV after the sample was exposed to 1 mbar O_2, **2)** after simultaneously exposing the sample to 1 mbar O_2 at 100 °C, **3)** and after simultaneously

exposing to 1 mbar O_2 at 150 °C. The primary change that takes place is in the O 1s spectra figure S7a where initially the higher energy contamination peaks increase after simultaneous O_2 exposure at 100 °C. The two Cu-O peaks at 530.4 and 529.5 eV also grow slightly at this point. However, a significant increase is seen in the 530.4 eV peak after annealing to 150 °C in 1 mbar O_2, while the contamination peak intensity remains mostly the same. Additionally, the N 1s and B 1s peaks are still present, suggesting the substrate surface was oxidized while the h-BN remained largely intact.

X-ray absorption spectroscopy (XAS) data were measured at each temperature and pressure throughout the experiment to determine the oxidation state of Cu. In figure S8 we show the total electron yield (TEY) for the Cu L-edge and O K-edge measured by collecting the sample current as the photon energy is swept. All spectra were normalized by collecting a calibration reference current measured with a photodiode. Baseline spectra were collected for h-BN/Cu(111) and a Cu_2O(111) single crystal prepared with a (1×1) surface.[93] Not much change is seen after initial exposures to 0.001 mbar of O_2 at UHV. After exposure to 1 mbar O_2 (blue), a peak is seen in the O K-edge corresponding to Cu^+. Once the sample was annealed to 100 °C (pink), this peak in the O K-edge decreases. When annealing to 100 °C in p_{O2} = 1 mbar (gold), the Cu L-edge shows an increase in the ratio of the rising edge peak at ~933 eV to the interference peaks that follow. Additionally, an increase is seen in the rising edge of the O K-edge, with evidence of a slight pre-edge reflecting the progressing oxidation of the surface region and consistent with Figure 3 from the main text. Following annealing to 150 °C (gray), the Cu L-edge shows a continued increase in the rising edge and decrease in interference peak intensities, along with the addition of a new interference peak at ~945 eV, showing strong similarity to the Cu_2O reference (purple). The O K-edge also shows a further increase in the rising edge and the addition of a new peak at ~542 eV that also agrees with the Cu_2O reference. The disappearance

of the pre-edge after annealing to 150 °C likely occurs as the surface grows a thicker oxide, relative to the well-ordered surface that has a distinct pre-edge peak seen in Figure 3.

(2) Preparation of a well-ordered Oxide

After the initial pressure and temperature dependence experiments, the recipe for preparing a relatively clean and ordered oxide underneath the h-BN layer was optimized. The order of the oxide was verified with LEED initially and discussed more in the main text. A further description of how the sample was prepared is located in the Methods section. XPS was utilized to show the chemical state changes throughout the preparation of the h-BN/$Cu_{2-x}O$/Cu(111) sample. The changes in high-resolution XPS are shown in figure S9, as the sample is transferred from the preparation chamber to the analysis chamber during each preparation step.

The O 1s spectra in figure S9a initially show adventitious species (black) followed by an slight increase in water after h-BN preparation (gray), likely due to a change in base pressure of the chamber (some high pressure experiments were performed after initial clean Cu(111) characterization). After oxidation (navy), the O 1s shows five visible peaks following peak fitting, agreeing well with previous spectra and literature.[56] The primary distinction between the prior pressure/temperature dependence experiments and the well-ordered oxide are the intensities of the surface oxide peaks at 529.5 and cluster peak at 530.4 eV. Previous measurements (figure S4 and figure S7), collected for oxidation during exposure to an x-ray beam and next to the cone, show a large increase in the 530.4 eV peak, suggesting further oxidation from the buildup of clusters, whereas the ordered oxide exempt from irradiation during oxidation has the largest increase in the 529.5 eV peak, corresponding to a thin film of surface oxide.[56] The presence of

excited oxygen generated from x-ray irradiation during prior measurements enhances the oxidation of the substrate.[68, 94-95]

The N 1s and B 1s spectra in figure S9b and c both show a Gaussian peak at 190.5 eV and 398 eV, respectively, along with a shoulder peak on the high BE side approximately ~0.6 eV higher the main peak.[26] The FWHM of the initial N 1s peak fit was constrained to 0.85 ± 0.05 eV to ensure the fitting software does not incorrectly assume one peak with a larger width. The small shoulder at the high binding energy side is due to defects in the h-BN lattice, as a similar shoulder is seen in both B 1s and N 1s spectra by Schwartz et al..[26] These defects are widely reported in the literature for h-BN, although the exact rationale is difficult to pinpoint. Generally, this shoulder represents parts in the h-BN layer where the B to N stoichiometry is no longer 1:1,[26] either from B or N vacancies, or H adsorption. Following the oxidation, both peaks shift approximately 0.3 eV to lower BE, while retaining the same peak shape. This 0.3 eV corresponds well to the difference in work function between Cu(111) (5.1 eV) and Cu_2O (4.8 eV) of ~0.3 eV.[57] We have also directly measured the work function, along with additional time dynamic photoemission studies for h-BN/Cu(111) and h-BN/$Cu_{2-x}O$/Cu(111) in a separate publication confirming this conclusion.[63]

Once again, the Cu 3p in figure S9d remains exactly the same throughout the preparation and oxidation, even for the clean Cu(111) surface and ordered Cu_2O-like oxide. This is likely due to the ratio of substrate Cu to the thin Cu_2O-like trilayer film that is expected to contain only two layers of Cu cations at the surface, making any oxidized Cu 3p contribution difficult to deconvolute. The C 1s in figure S9e shows little to no growth of oxidized carbon species relative to the increase seen from previous experiments, which was likely due again from exposure to excited oxygen. After oxidation, the C signal decreases as some of the carbon is burned off through oxidation, which also explains why the B 1s and N 1s signals slightly increase.

Additionally, the C 1s displays the same ~0.3 eV shift that the B and N spectra show, consistent again with the change in work function of the substrate. Prior to this, a shift is also seen in the C 1s of ~0.8 eV, which is consistent with the lower work function of the h-BN/Cu(111) compared to Cu(111). The valence level in figure S9f also shows after oxidation a slight increase in the intensity in the region between the d-band edge at ~2 eV binding energy (blue arrow), along with a decrease at ~4 eV (red arrow), which is expected for oxidized Cu.[96-97]

Using the Simulation of Electron Spectra for Surface Analysis (SESSA) Version 2.2 software, we simulated the relative intensities of each core level from a survey spectrum shown with the measured survey in figure S10a.[98] A sample layer shown in figure S10b was designed with a Cu substrate (11 valence electrons, 1 atom/molecule, 8.5×10^{22} atoms/cm^3, and infinite thickness), a 3.75 Å thick Cu_2O thin film based on the Cu_2O lattice where one trilayer is 2.5 Å and an additional 1.25 Å between two Cu planes to account for the chemisorbed O[76] (28 valence electrons, 3 atoms/molecule, 7.6×10^{22} atoms/cm^3, and 2.1 eV bandgap), a 4.5 Å thick h-BN thin film where the 3.1 Å Van-der-Waals gap is added to the molecular thickness of a N atom at 1.4 Å[99] (8 valence electrons, 2 atoms/molecule, 9.2×10^{22} atoms/cm^3, and 5.9 eV bandgap), and finally a 1.5 Å thick adventitious carbon layer on top (4 valence electrons, 1 atom/molecule, 1.1×10^{22} atoms/cm^3, 0 eV bandgap). All 1s peak types were set to Gaussian shapes, while the Cu 3p was set to a Lorrentz shape due to the broad peak shape seen in measured spectra. All Auger peaks were also set to Lorrentz shapes. Peak positions and widths were set based on the measured data. Cross sections and inelastic mean free paths were not adjusted and the software default for each atom input was used. A photon source of 720 eV with 100% linearly polarized light was used to match the synchrotron experiments from the PEARL endstation. The geometry for the PEARL endstation was also used, with a 60° source to analyzer angle, normal emission, and 90° orientation of the polarization vector, detected with a Concentric Hemispherical

Analyzer (CHA).[73] The simulation was set to a convergence factor of 1×10^{-2} using the surface excitations model and auto set for number of collisions and trajectories. To compare with the measured data, the simulated values were normalized to the Cu 3p spectra and offset. A reasonably good agreement to the measured spectra is seen with the ratios of each core level to the Cu 3p.

In addition to the "5 min" oxide, we also prepared a "35 min" oxide using the same exposure conditions and simply exposing the sample for an extra 30 min. A comparison of the XAS for the freshly prepared h-BN/Cu(111), the "5 min", and "35 min" oxide is shown in figure S11. The N K-edge and B K-edges in figure S11a and c are consistent throughout all the h-BN samples and resemble high-resolution XAS data for h-BN films, showing both the σ* and π* peaks reported in the literature.[48] In addition, we simulated X-ray adsorption spectra for N and B on different substrates (figure S11b and d) with the Perdew-Burke-Ernzerhof (PBE) exchange-correlation functional. In both heterostructures, B K-edge exhibits two edge features at 193.0 and 199.5 eV, and two edges for the N K-edge at 402.4 and 408.7 eV, respectively. It is expected that the calculated energy will be slightly offset from the measured spectra, however the peak shapes and distances between peaks are of greater interest. The small peaks in the h-BN/Cu(111) simulations (red) before the lowest energy N K-edge and after the lowest energy B K-edge should be attributed to the hybridization on Cu(111), which agrees well with the observations in projected density of states (PDOS) shown in figure S14. However, they do not alter the staple characteristics of the π^* and σ^* in XAS, therefore, we conclude that in both cases the h-BN is physisorbed and its structural and electronic properties are not significantly affected by the substrate. Furthermore, we see the same change in the pre-edge of the N K-edge for the measured data as well as a slight change in the slope after the edge, highlighted by two black arrows in figure S11a. **This offers the strongest argument that the oxide is indeed**

intercalated and confined beneath the h-BN layer, otherwise we should still see these hybridization peak features in the N K-edge if we were only able to oxidize patches of exposed Cu not covered with h-BN. Unfortunately, we cannot see much of a difference in the B K-edge due to a low resolution after the π^* edge. The intensity of the π^* edge is very large relative to the baseline and only a few data points are collected afterwards with a 0.2 eV step size to account for the length of the scan.

The O K-edge figure S11e for both the "5 min" and a further oxidized "35 min" preparation shows a pre-edge at ~529.4 eV, corresponding to the chemisorbed oxygen. The XAS for the "35 min," corresponding to a more bulk-like oxide, displays a peak at 531.9 eV that is also present for the "5 min" oxide but significantly more intense. Additionally, these spectra are plotted as overlays to highlight the same intensity of the pre-edge, due to a saturation of chemisorbed O sites on the Cu surface. DFT was also used to simulate the XAS spectra shown in figure S11f for each of the O atoms in the model structure from figure S19 with the PBE exchange-correlation functional. Again, the peak positions are slightly underestimated from the measured data, but peak shape and distance between the pre-edge and rising edge are respectively similar. The O from the upper and lower layers of the trilayer have analogous yet slightly different peak positions, which can be assumed to be additive in the measured spectra, forming the O-Surf [$Cu_{2-x}O$] (brown) spectrum in figure S11f. The significant increase in the "35 min" at 532 eV suggests additional $Cu_{2-x}O$ oxidation, which could come from a thicker film (several stacked trilayers) or a buildup of clusters that should have a similar coordination to Cu atoms as the trilayer O. While we see an obvious change in the O K-edge between the oxidation times, essentially no change is seen in the Cu L-edge from prior to oxidation to "5 min" exposure. Once "35 min" is reached, a slight shift in the rising edge occurs and the presence of two peak bumps are seen that correspond to Cu_2O.

An XPS depth profile of the O 1s was executed using various photon excitation energies and emission angles. The data are plotted normalized to the low binding energy background for a visible comparison that accounts for the difference in signal intensity relative to the background. In figure S12b and c, we show the comparison of the "5 min" and "35 min" oxidation for 720 eV and 1500 eV photon excitation energy, corresponding to 185 eV versus 975 eV KE for the emitted electrons. This provides a difference in attenuation through Cu of ~10 Å, where the 720 eV is extremely surface sensitive. Comparing the "5 min" oxidation in figure S12a, we see the primary difference is for the 1500 eV, more of the cluster signal (green) and less of the carbon (purple) and hydrogen (teal) peaks are seen. A similar increase in the same peaks is seen for the longer oxidation of "35 min" in figure S12b. As we see the 1500 eV for the "35 min" in figure S12c, the cluster peak (green) is now larger than the surface oxide (red). The grazing versus normal emission for the "5 min oxide" at 720 eV shown in figure S12d is rather intriguing, as one would expect to see more or at least a similar ratio of clusters to surface oxide as we get more surface sensitive with grazing emission. When we go from normal (0°, black) to grazing at 80° emission (gray), the ratio of peaks stays nearly the same, as expected. However, at 90° emission (navy), the surface oxide drastically decreases while the cluster peak slightly increases, which suggests that the clusters can protrude the h-BN, as evidenced by the STM and depicted in figure S13. These clusters can act as a shadowing effect that can significantly dampen the signal for the surface oxide as the electrons now attenuate through the clusters. For the 1500 eV excitation, the cluster signal also increases because we can see deeper into the cluster, providing a larger signal than the 720 eV. As the sample is further oxidized, more clusters coalesce, thus also increasing this signal for the "35 min." In figure S12e and f, we display the normal and maximum grazing emission (polar angle of 90°) data collected for N 1s and B 1s, respectively. For both the N 1s and B 1s, no change is seen between the ratio of the main peak to the defect

peak for normal and grazing, suggesting the h-BN layer is reasonably uniform and no oxidized B or N are present.

To better understand the cluster structure and the electronic changes we would expect with oxidation, we used DFT to calculate the absolute interaction energy (E_{int}) per BN atom pair on different substrates, namely Cu(111) and oxidized $Cu_{2-x}O$/Cu(111) at the PBE+D3 level. E_{int} is obtained from Equation 1.

$$E_{int} = \left[E_{tot} - \left(E^f_{sub} + E^f_{hBN}\right)\right]/N_{BN}, \quad (1)$$

E_{tot} is the total energy of the relaxed heterostructure (i.e. h-BN covered substrate), N_{BN} is the number of BN pairs in the supercell of the heterostructure, E^f_{sub} and $E^f_{h\text{-}BN}$ are the total energies of the individual subsystems (e.g., Cu(111) slab or oxidized $Cu_{2-x}O$/Cu(111) with chemisorbed O as substrate and free standing h-BN) taken with the coordinates of the fully relaxed heterostructure. This implies that the subsystems in this case have not been individually optimized and the calculated energy difference corresponds to a net interaction energy and not to an adsorption energy. The interaction energy of h-BN with the substrate is rather weak, and changes only slightly from –0.150 per BN pair on Cu(111) to –0.086 eV per BN pair on $Cu_{2-x}O$/Cu(111) with chemisorbed O. In analysis of the electronic properties by means of PDOS (figure S14), there is clear hybridization of Cu_d and N_p orbitals at -2 eV, corresponding to filled states (figure S14a,c,e). Due to the closer interaction between h-BN and Cu(111), a few electrons transfer from the Cu(111) surface to h-BN and occupy N_p orbitals, resulting in the Fermi level moving towards to the conduction band in h-BN/Cu(111) heterostructure. Though isolated h-BN should have a wide band gap and no states at the Fermi level, there is a tiny state at both N_p and B_p hybridizing with Cu_d, which indicates a stronger interaction with Cu(111) than the oxidized substrate. In the right panels (figure S14b,d,f), after oxidation, these electrons prefer a deeper

valence state, which is hybridized with O_p around -8 to -6 eV rather than B or N orbitals. Thus, the hybridization between Cu_d and N_p decreases, and h-BN remains with a larger band gap of about 4.5 eV. This also agrees well with measured valence band measurements done in a separate study by our group.[63] We can see from the projected DOS (figure S14g-j), that chemisorbed O, O_u and O_l have distinguishable p-states (around –8 to –4 eV), indicating their different chemical environments. Interestingly, chemisorbed O atoms in the Cu_{hcp} and Cu_{fcc} sites have nearly indistinguishable PDOS profiles. Additionally, we can see from figure S14f, that the presence of a h-BN covering layer has no discernible effect on the states of O atoms, corroborating that h-BN is not covalently adsorbed and transparent, with minimal impact on the electronic properties of the underlying substrate.

Using the relaxed h-BN/$Cu_{2-x}O$/Cu(111) cluster with O-Cu_{fcc}, we simulated STM intensity plots shown in figure S15 to compare with the measured data collected at -2.5 eV for a range of -1 to -3 eV sample biases, corresponding with filled states. The -2.5 eV sample bias is probing the Cu_d states at -2.1 eV relative to the Fermi level, seen in Figure S14f. We added a blur to the simulated STM to compare with the lower resolution experimental data, and overlayed several unit cells of simulated plots with the full measured STM.

XPD diffractograms were also collected to obtain information on the structure of the h-BN/$Cu_{2-x}O$/Cu(111) heterostructure. In figure S16 we plot experimentally collected XPD patterns of the O 1s core level, highlighted from collected spectra shown in figure S16a. To reduce the number of fitting parameters in extracting intensities from individual spectra, the chemisorbed oxide peak (blue) is constrained in a 1:6 intensity ratio to the surface oxide peak, based on the model presented in Figure 2. Therefore, the surface oxide yields only one pattern in figure S16b. Interestingly, the cluster peak (green) shows a distinct pattern in figure S16c, suggesting the clusters have some homogeneous structure that clearly shows three-fold

symmetry. The copper oxide clusters are expected to be conglomerated facets forming a vertical pyramid structure depicted by Gloystein et al..[60] Therefore, even though the surface is not homogenously covered with clusters, we can still see a diffraction pattern for these clusters as long as the cluster structure and orientation are uniform.

If we focus on the anisotropy (defined as [$A = (I_{max} - I_{min})/I_{max}$], where I corresponds to the gray space intensity) for the O 1s XPD, we see A = ~50%, indicating that a large part of the oxygen atoms belong to an ordered oxide phase. XPD patterns of the Cu 3p, N 1s and B 1s were also collected and displayed in figure S17, together with EDAC simulations for a h-BN covered $Cu_{2-x}O$/Cu(111) surface and an unoxidized h-BN/Cu(111) surface. They show rather good agreement between experiment and simulations, as well as similarities to literature results for h-BN on Ni(111) and Gr/h-BN/Cu(111),[66, 73] where the primary differences are slightly more distinct pattern features in the unoxidized sample and a small difference in intensity contrast.

Finally, we utilized the same slab coordinates used for DFT for simulating XPD patterns with the EDAC code. In figure S17, all the measured XPD patterns (a, h, l) collected for the "5 min" oxide at the PEARL endstation are shown along with the simulated patterns using figure S19b, 19i, and 19m. All patterns were calibrated for the grayspace shown by the scale to the right. The input parameters for the simulations are described in the materials and methods section. The Cu 3p (a), B 1s (h), and N 1s (l) are shown with a three-fold average due to the three-fold symmetry of the Cu(111) substrate. A near perfect agreement with the simulated Cu 3p can be seen in (b). The B and N 1s measured patterns show evidence of six-fold symmetry, which is confirmed when 6-folding the simulated patterns. This suggests there are rotational domains at 30° relative to normal in addition to the three-fold symmetry from the h-BN/Cu unit cell. To decrease simulation expense, we only used two Cu layers below the h-BN film. A distinct difference is seen between the two simulated Cu 3p patterns, where the 4 Cu layers in the

"5 min oxide" much more closely resemble the measured data. This should have a limited effect on the B 1s and N 1s patterns, and therefore satisfactory for comparison with measured B 1s and N 1s patterns. Ultimately, O 1s XPD was unable to fully verify our model, due to multiple oxide phases present in the large unit cell needed for simulations. Regardless, the B 1s and N 1s XPD are able to provide further confirmation of the h-BN quality above an ordered oxidized substrate.

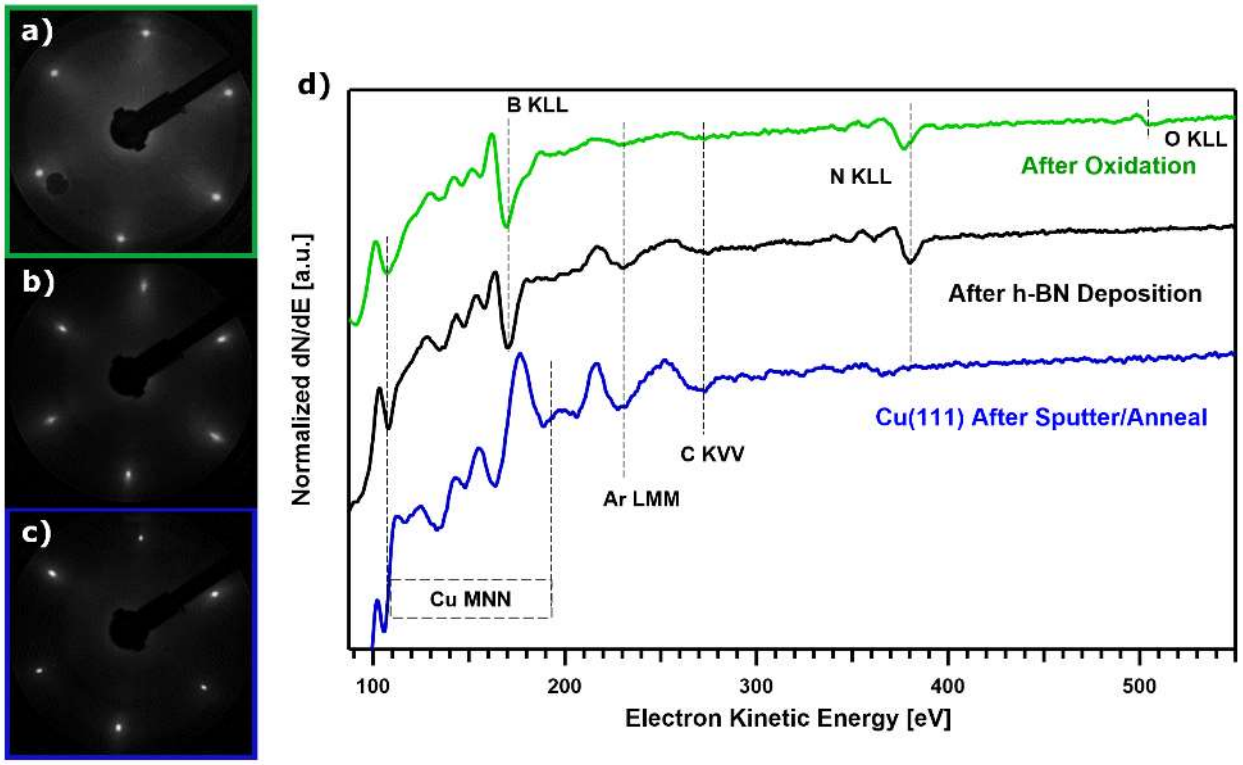

figure S1. LEED images taken with 70 eV electron excitation energy of a) h-BN/$Cu_{2-x}O$ /Cu(111), b) h-BN/Cu(111), and c) Cu(111). AES spectra of all three sample preparations shown in d, where the spectra colors correspond with the boxed LEED images on the left.

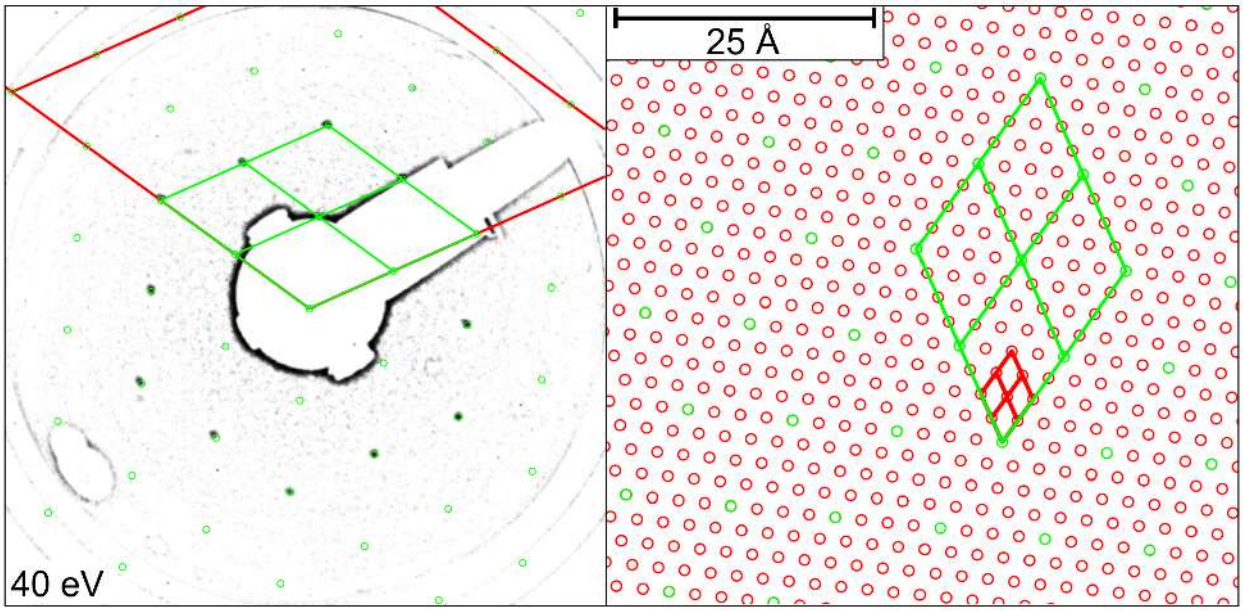

figure S2. LEED image of h-BN/$Cu_{2-x}O$/Cu(111) using 40 eV electron excitation energy. The diffraction spots show the (4×4) overlayer structure of chemisorbed oxygen, corresponding to the 10.2×10.2 Å unit cell seen in Figure 1c,d. To the right, the real space image is shown of the corresponding LEED space structure.

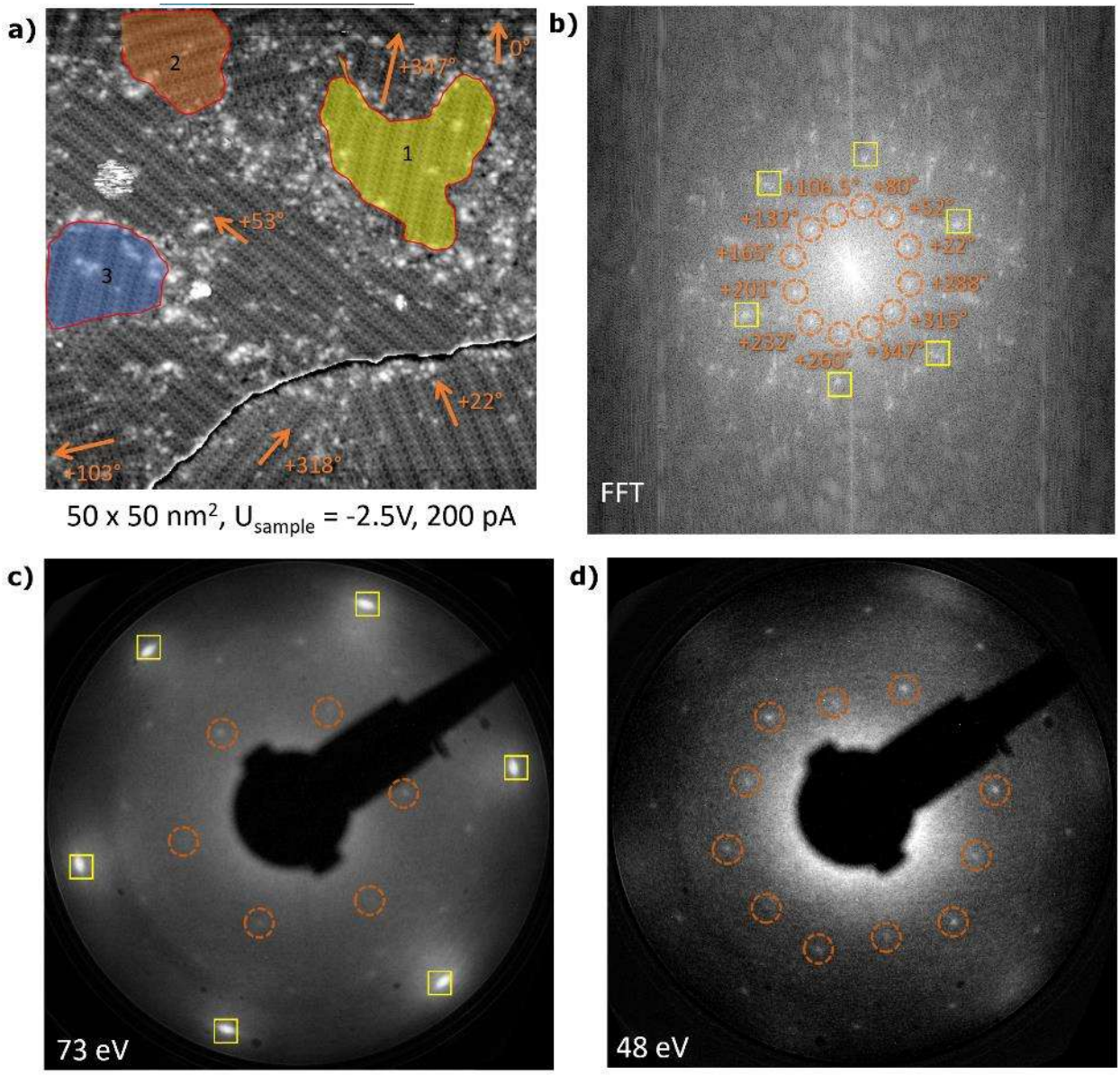

figure S3. (a) Real-space image (as shown in Figure 1b in the main text), with three of the many h-BN grain boundaries highlighted in yellow, orange, and blue. The fast Fourier transform (also shown in Figure 1c) is shown again highlighting specific diffraction spots that correspond to the spacing in the LEED images at 73 eV (c) and 48 eV (d). Twelve diffraction spots are highlighted in orange dashed circles, exhibiting a mutual rotation by 30° ± 2°. Domains with the same mutual rotation can be identified in the real-space image (a), where five selected domains are highlighted by orange lines parallel to the bright, row-like features in individual domains.

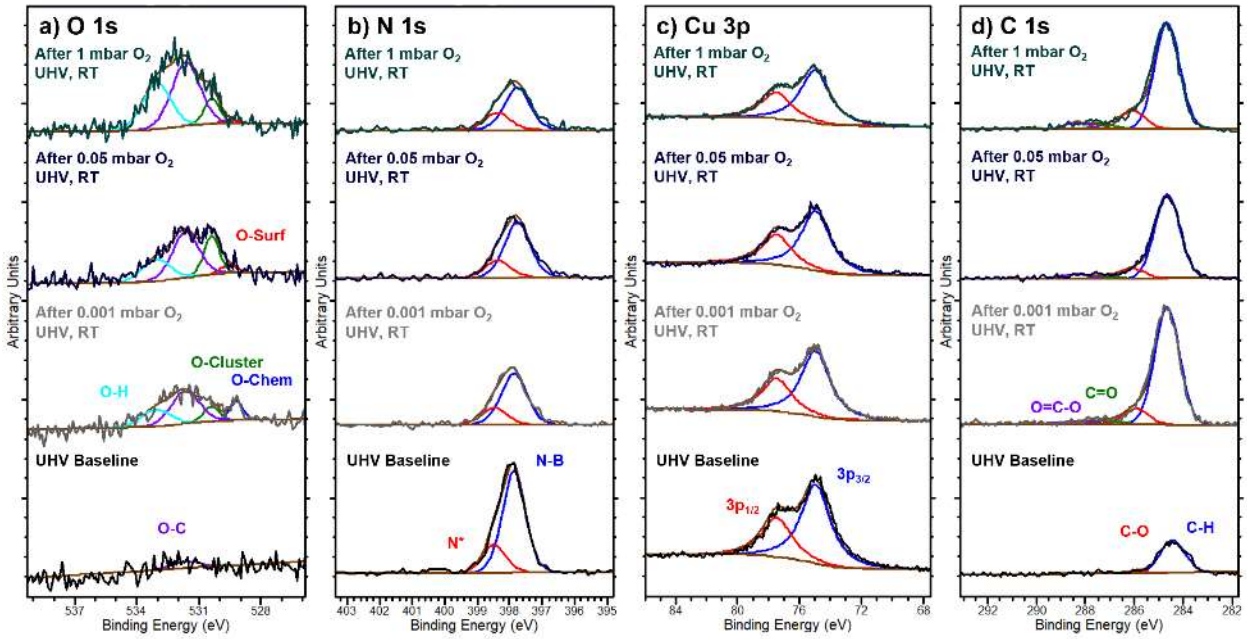

figure S4. APXPS measurements at *hv* = 700 eV displaying the pressure dependence of O_2 intercalation for h-BN/Cu(111). Initial baseline spectra at UHV and room temperature (RT) are shown in black, along with measurements at p_{O2} = 0.001 mbar (gray), p_{O2} = 0.05 mbar (navy), and p_{O2} = 1 mbar (green) for O 1s (a), N 1s (b), Cu 3p (c), and C 1s (d). B 1s is excluded due to an overlap of the O KLL using *hv* = 700 eV.

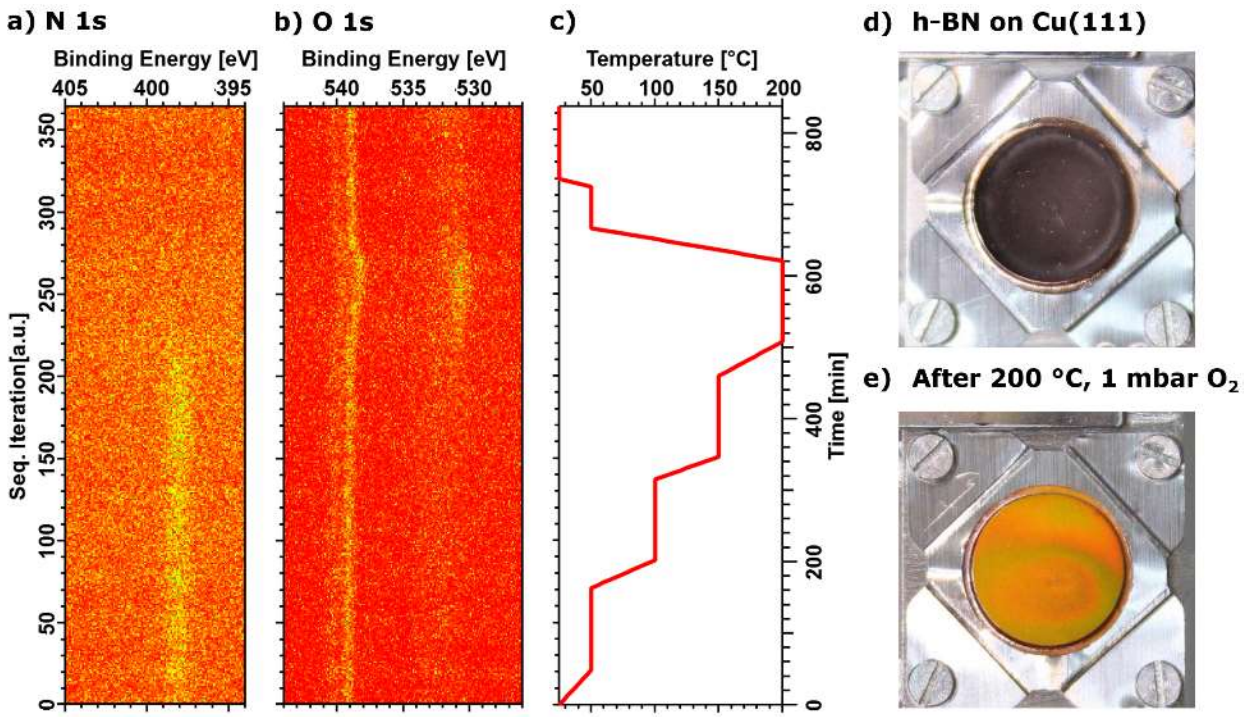

figure S5. Thermal stability of h-BN/Cu(111) measured using time-lapsed APXPS. Sequential iterations of the N 1s (a) and O 1s (b) are shown alongside increasing temperature with respect to iteration (c). Macroscopic pictures of the sample surface are also shown before (d) and after (e) exposure to 200 °C and p_{O2} = 1 mbar for ~100 min.

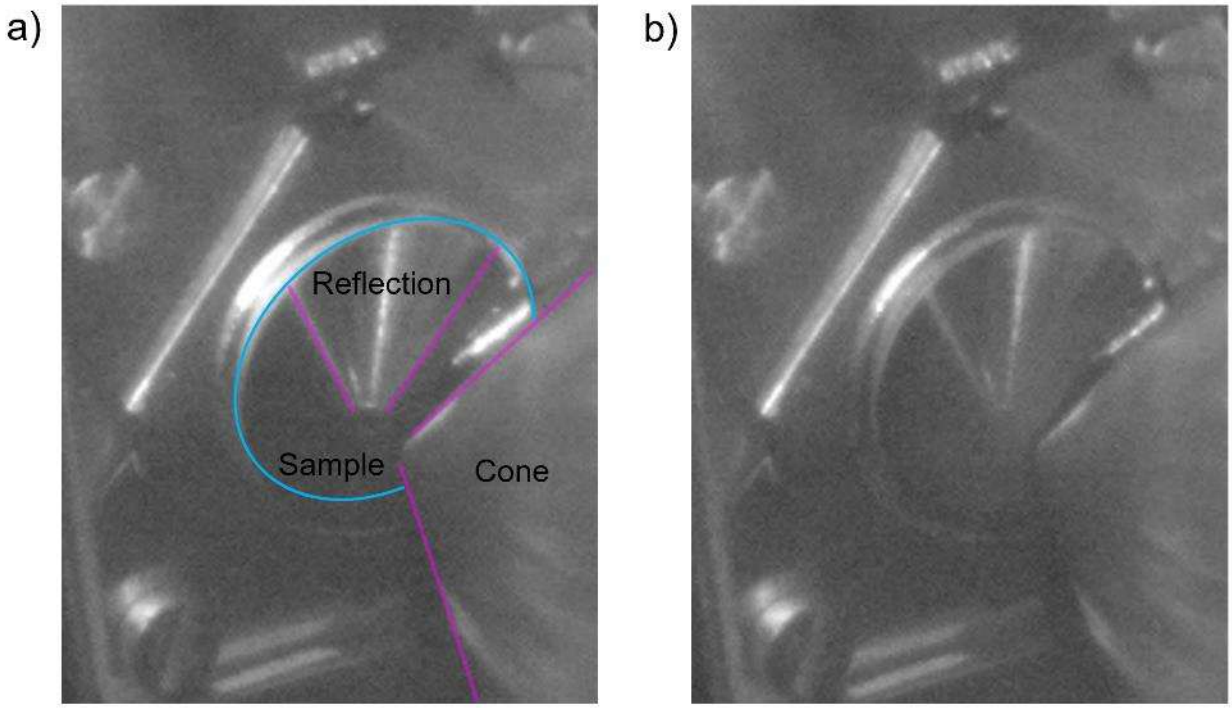

figure S6. Grayscale images of the h-BN/Cu(111) sample before (a) and after (b) anneal to 150 °C at 1 mbar O_2 partial pressure. A faint change in the surface optical properties is seen after exposure where the cone entrance orifice is no longer visible.

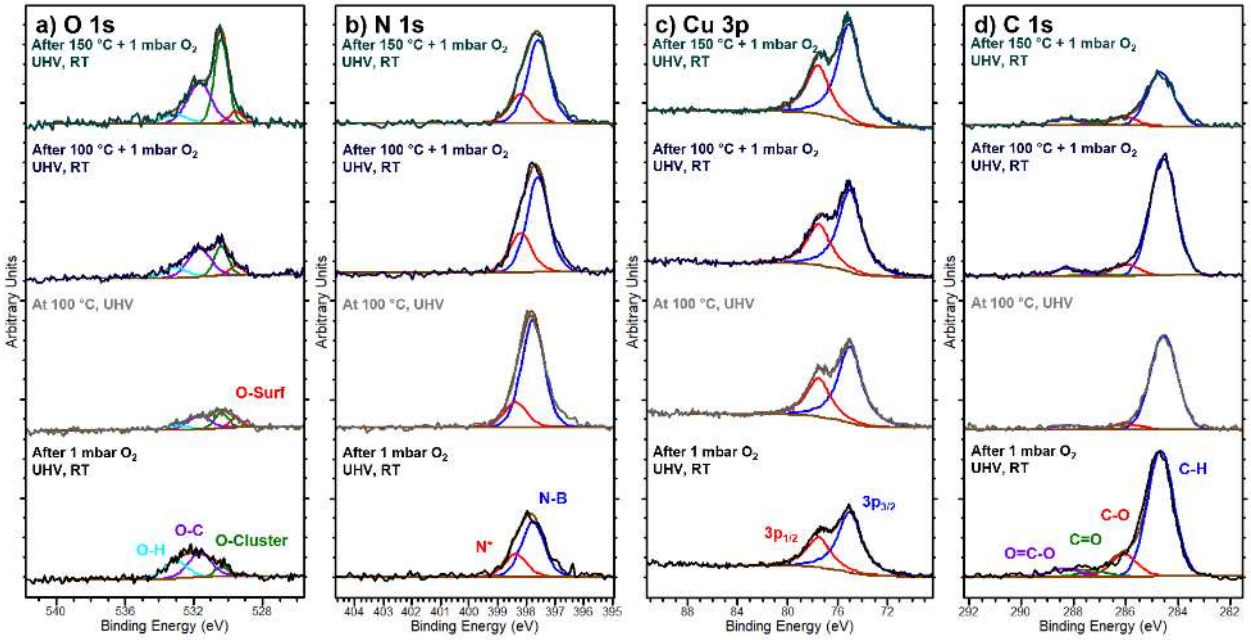

figure S7. APXPS spectra of O 1s (a), N 1s (b), Cu 3p (c), and C 1s (d) collected with $h\nu$ = 700 eV (again B 1s excluded due to O KLL overlap). Initial baseline after exposure to p_{O2} = 1 mbar (green spectra from figure S4) is shown in black. The sample was annealed to 100 °C and held at temperature for XPS (gray). While at temperature, p_{O2} = 1 mbar was backfilled for ~3 hours and then purged to UHV and cooled to RT (navy). This same procedure for navy was repeated but now annealing to a total of 150 °C (green) only for ~1.5 hours when it was noticed from the CCD camera (figure S6) that the sample was oxidized.

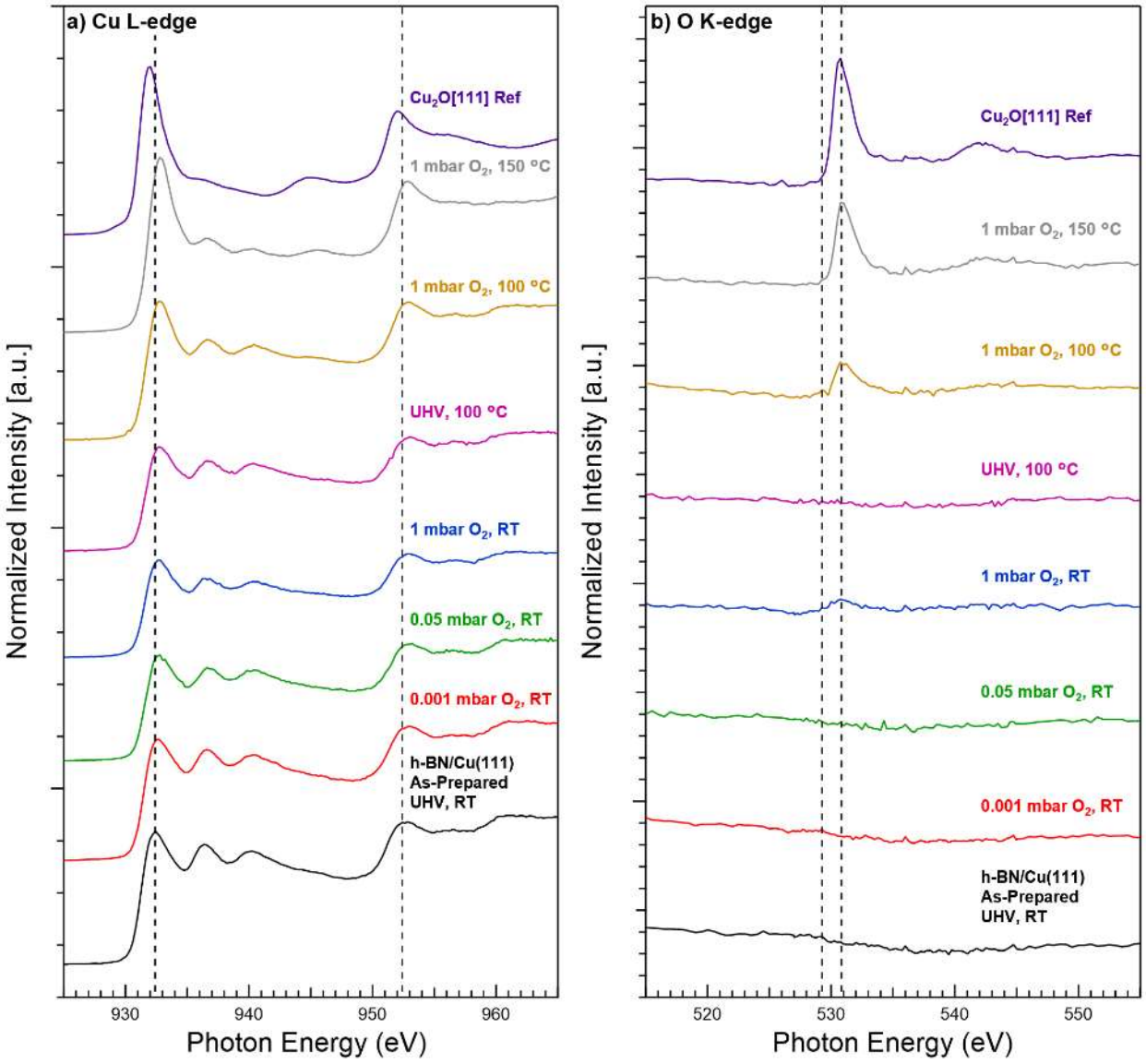

figure S8. X-ray absorption spectra showing the temperature and pressure dependence of oxygen intercalation of h-BN/Cu(111). The total electron yield was measured *via* the current through the sample for the Cu L-edge (a) and O K-edge (b).

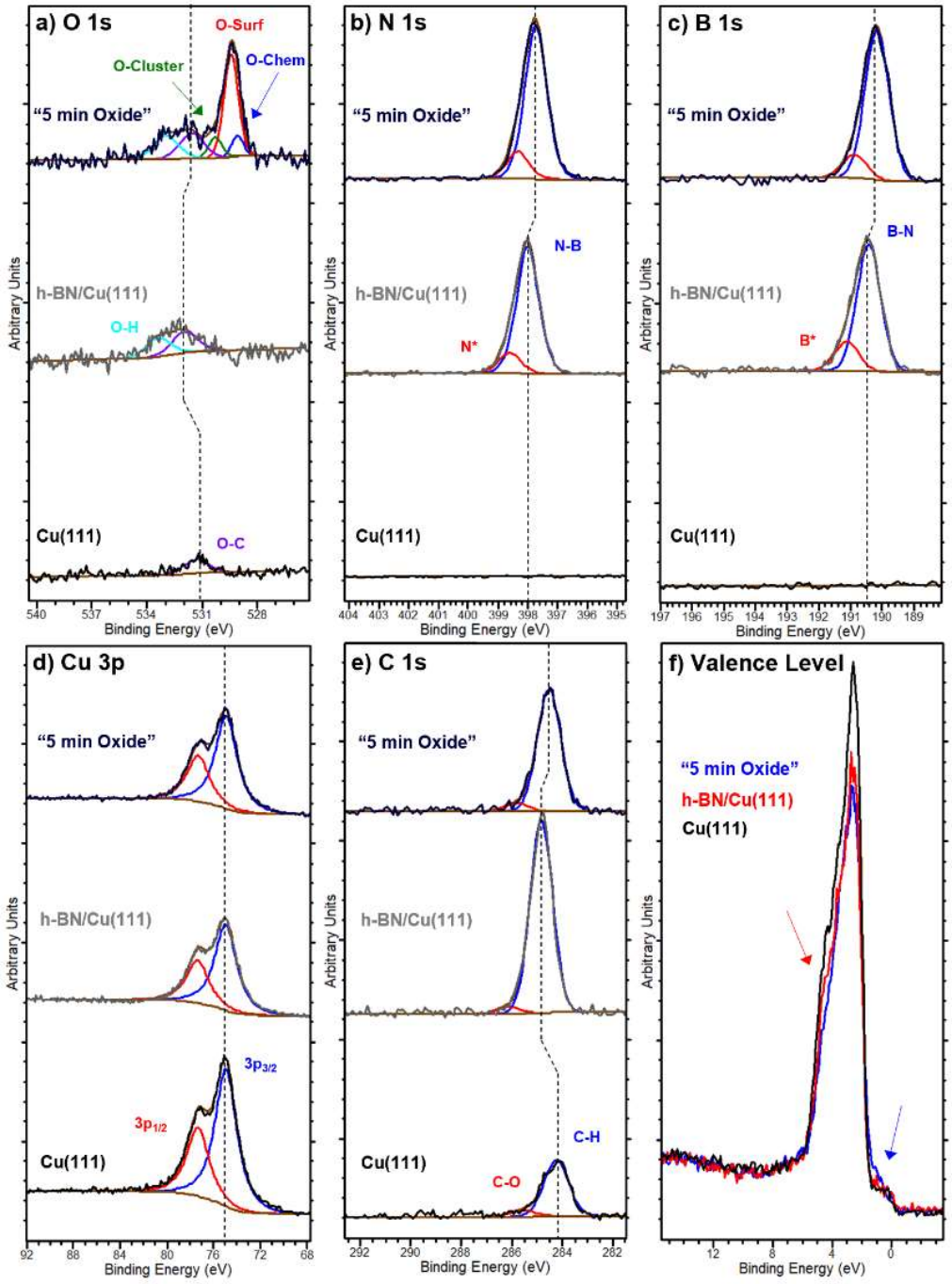

figure S9. XPS data for 3 separate sample preparations, Cu(111) (black), h-BN/Cu(111) (gray), and the "5 min oxide" (navy), all done sequentially on the same sample for the B 1s (a), N 1s (b), Cu 3p (c), O 1s (d), and C 1s (e) core levels, as well as the valence level (f). The dotted lines highlight the small shift in BE due to changes in the sample work function with each preparation.

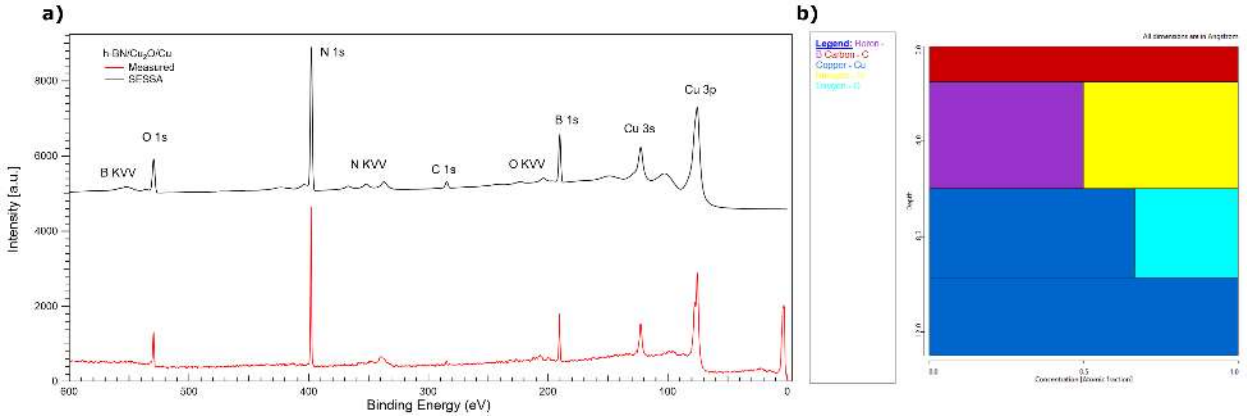

figure S10. (a) Comparison of measured XPS survey (red) and a simulated survey using the SESSA software. (b) Cross section of the concentration model used for input into the SESSA simulation.

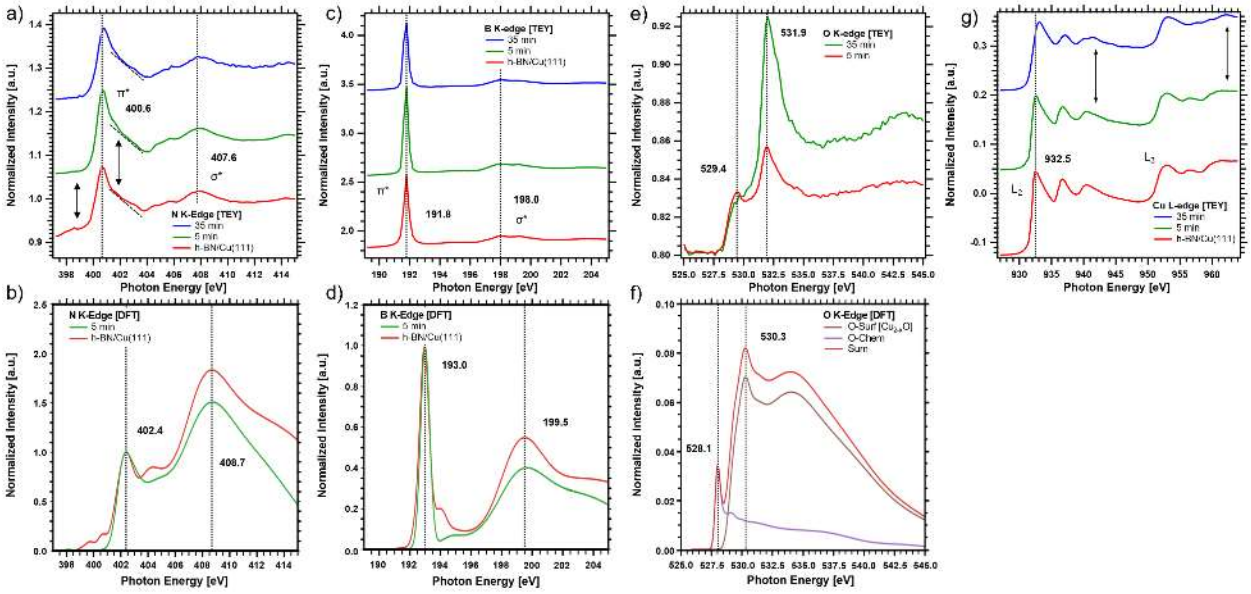

figure S11. X-ray absorption spectra of the ordered h-BN/$Cu_{2-x}O$/Cu(111) heterostructure prepared *via* oxidation at 1 mbar O_2 at 150 °C for 5 and 35 minutes, respectively. Spectra were collected at room temperature and UHV for the N K-edge (a), B K-edge (b), O K-edge (c), and Cu L-edge (g). Simulated XAS from the DFT model of bare h-BN/Cu(111) in figure S18 (red) and the oxidized slab in figure S19 (green) are also shown for the N K-edge (b), B K-edge (d), and O K-edge (f). The chemisorbed O (purple) in (f) corresponds to the O-Cu_{FCC} atoms, while the O_l and O_u (brown) correspond to the added intensity of the lower- and upper-layer O atoms, respectively. All three O atom intensities are summed shown in red.

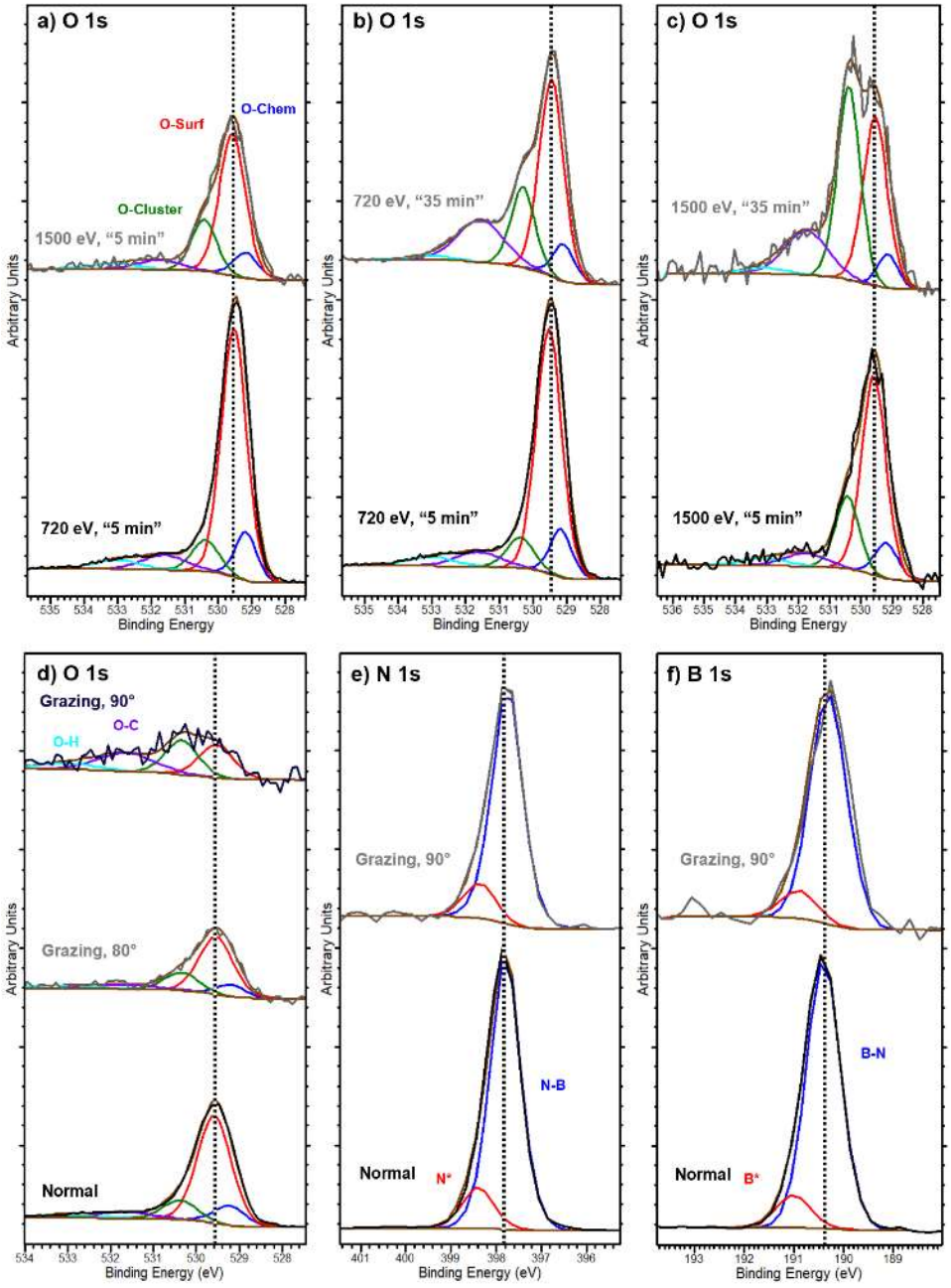

figure S12. XPS of O 1s comparing 720 eV and 1500 eV photon excitation energy (a), corresponding to 185 eV versus 975 eV KE for the emitted electrons, respectively. A longer oxidation of "35 min" is compared with the "5 min" oxidation with 720 eV (b) and 1500 eV (c). Normal versus grazing emission XPS using 720 eV photon excitation energy for the "5 min" sample shown in (d). Normal and grazing emission of N 1s (e) and B 1s (f) with 720 eV is also shown.

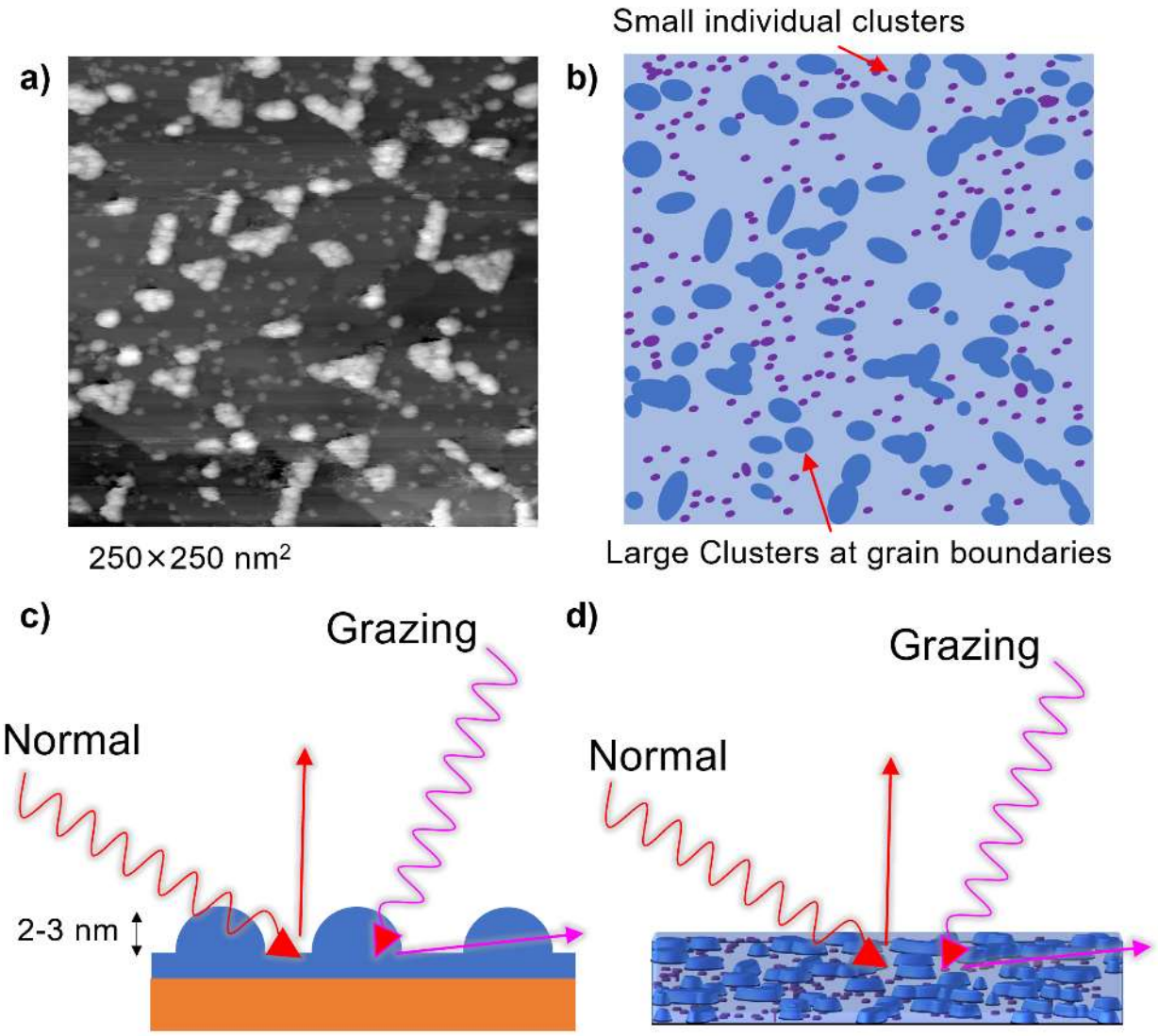

figure S13. STM image of a longer 35 min exposure to 1 mbar of O_2 at 150° with 250×250 nm^2 resolution (a) and a cartoon depiction highlighting the difference in clusters (b), where the dark blue are 2-3 nm conglomerated clusters, and the purple are small individual clusters. A depiction of how this affects the XPS signal for grazing versus normal emission is shown from a 2D (c) and 3D (d) perspective.

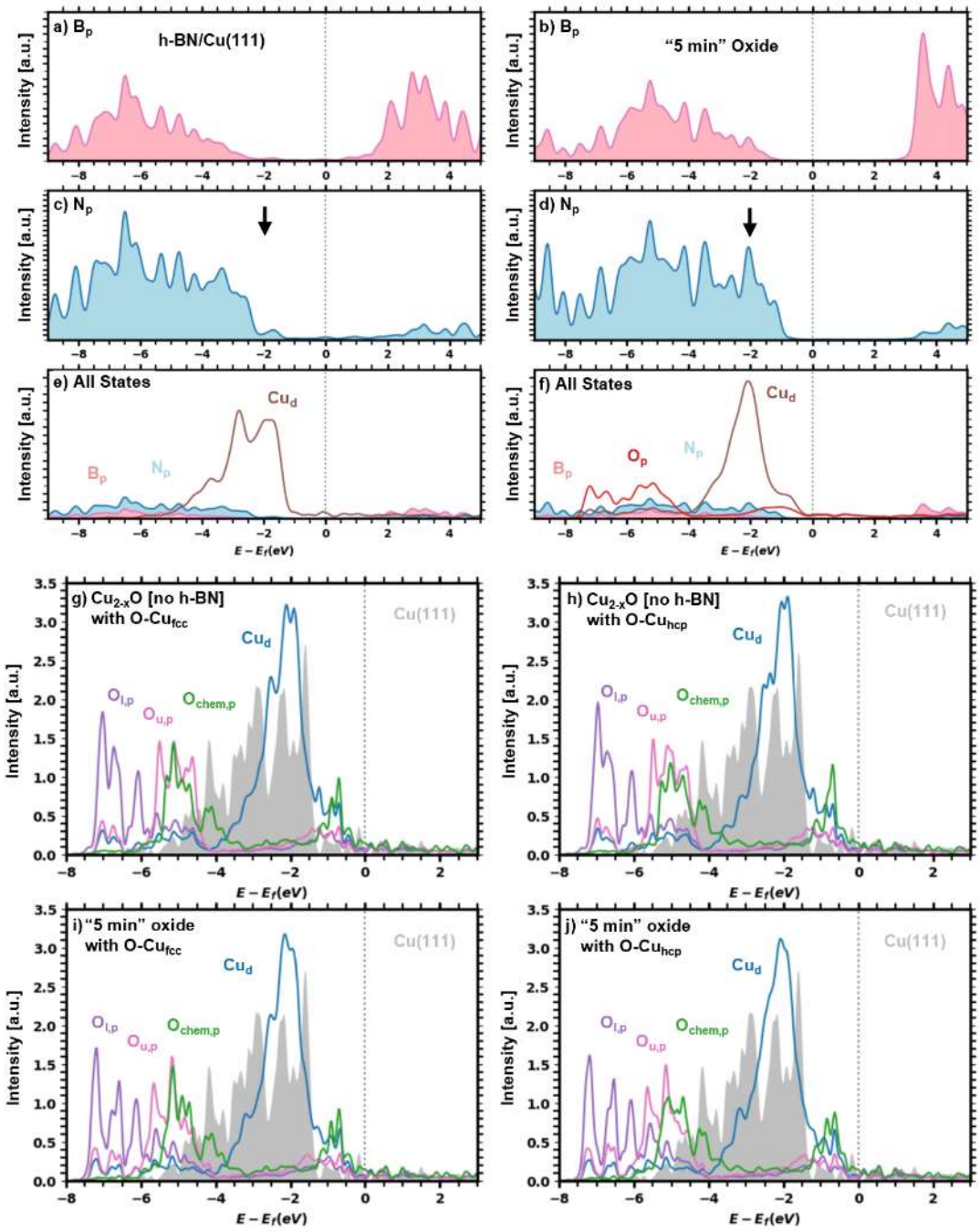

figure S14. PDOS aligned to the Fermi level of each heterostructure, showing the contribution from the p-states of B (a), N (c), and d-states of Cu (e) for h-BN/Cu(111). After "5 min" oxidation, the p-states of B (b), N (d), O p and Cu d-states (e) are shown. The comparison of Cu d and O p states are shown for $Cu_{2-x}O$ with no h-BN (g,h) and with h-BN (i,j) for when O chemisorbs to an O-Cu_{fcc} site (g,i) and an O-Cu_{hcp} site (h,j).

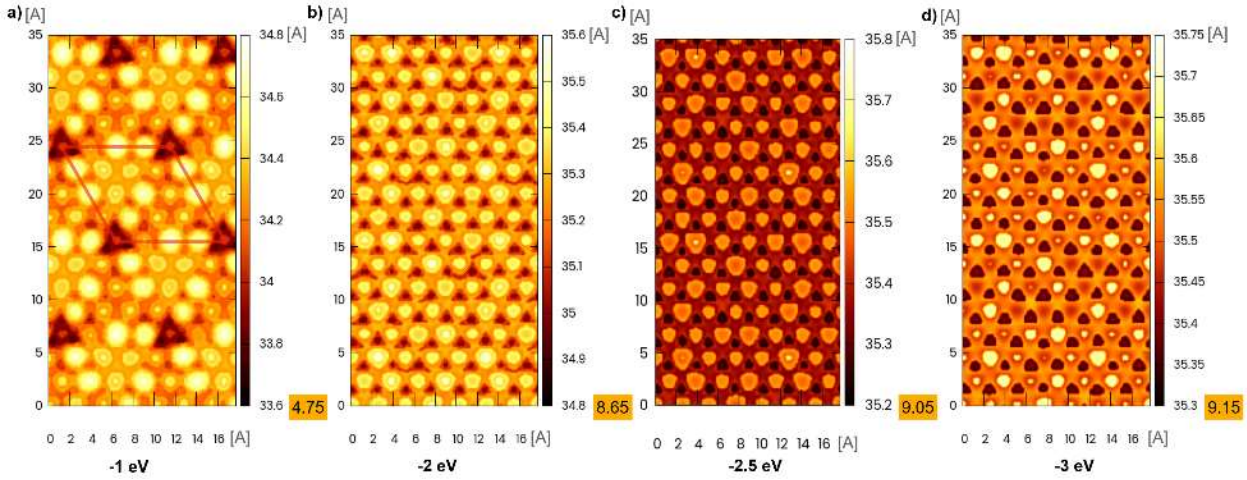

figure S15. STM from the DFT calculated DOS of the periodic h-BN/$Cu_{2-x}O$/Cu(111) slab with chemisorbed O atoms, shown in figure S19. This was simulated for negative sample biases of -1 eV (a), -2 eV (b), -2.5 eV (c), and -3 eV (d). The low intensity dark holes are the center of a h-BN hexagon. The triangle like shape in the -1 eV corresponds to the chemisorbed O, which a unit cell can be drawn in red. Depending on the position of the Cu and O beneath the B and N atoms provides the varying intensities.

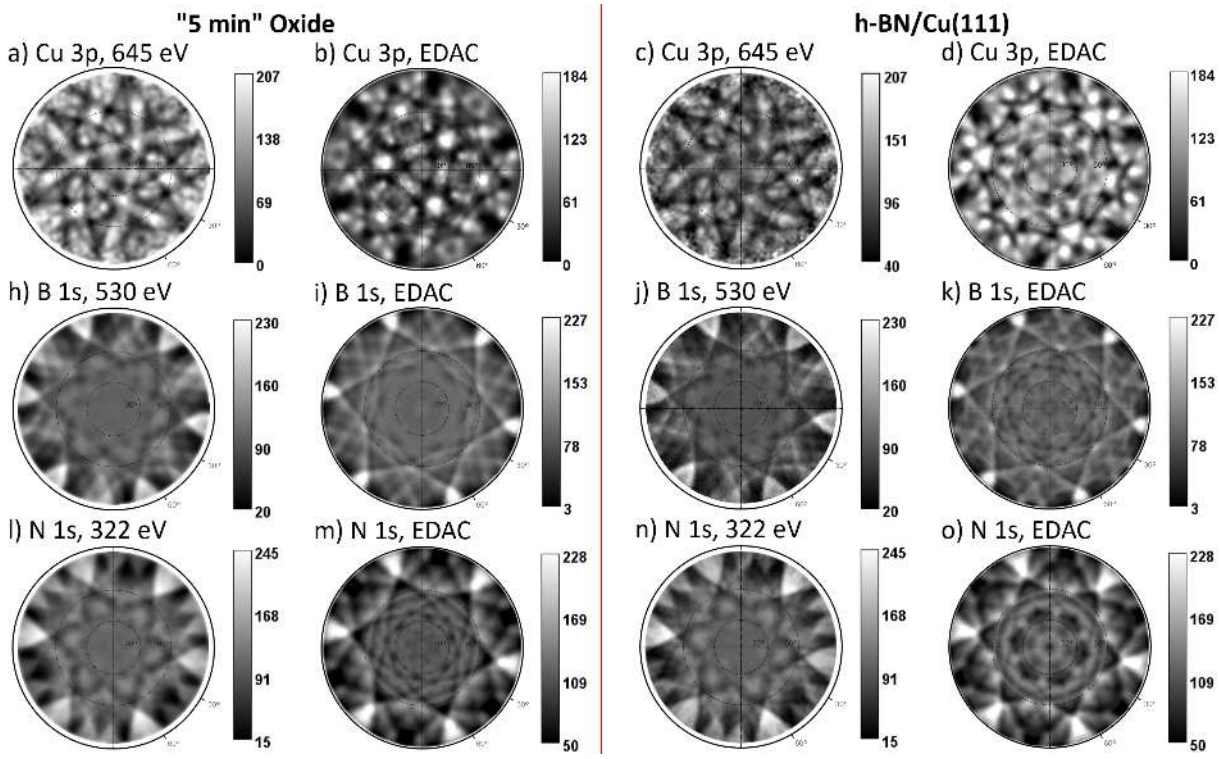

figure S16. Experimental XPD patterns of the "5 min" (left) and unoxidized (right) preparation for Cu 3p (a, c), B 1s (h, j) and N 1s (l, n). EDAC simulations using the clusters shown in figure S18 (h-BN/Cu(111)) and figure S19 ("5 min" oxide) are shown alongside the measured data and the corresponding KE for Cu 3p (b), B 1s (d), N 1s (f), and O 1s (h) using an excitation energy of 720 eV. All simulations are rotated 40° to align with the direction of the measured Cu substrate.

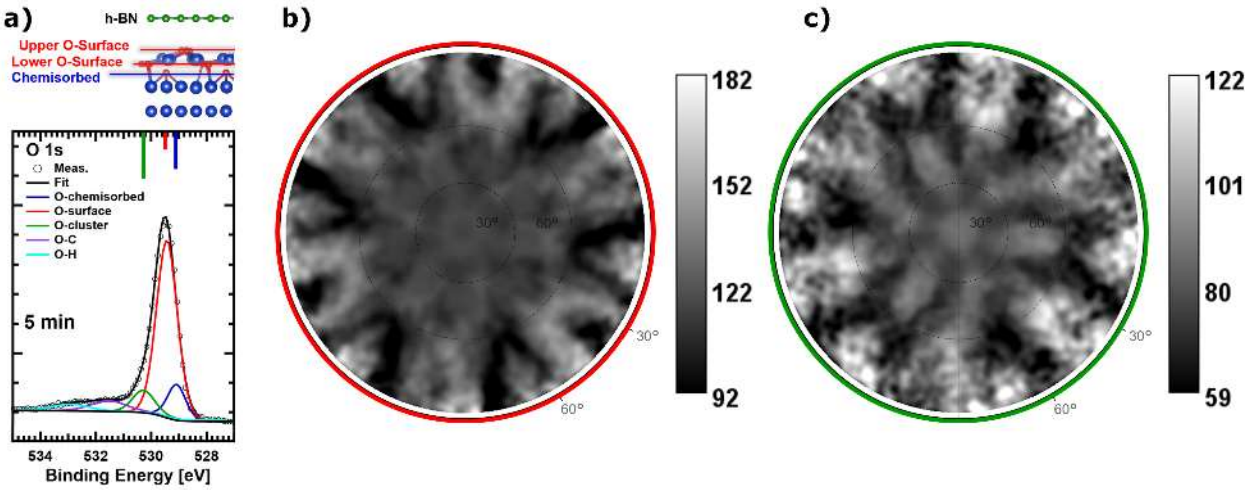

figure S17. XPD plots of the h-BN/$Cu_{2-x}O$/Cu(111) heterostructure for O 1s corresponding to the O 1s peak fit (a). O-surface (b, red) and O-cluster (d, green) are experimentally measured XPD patterns collected with a photon excitation energy of hv = 720 eV. The large anisotropy of each suggests a large part of the O atoms belong to an ordered oxide phase.

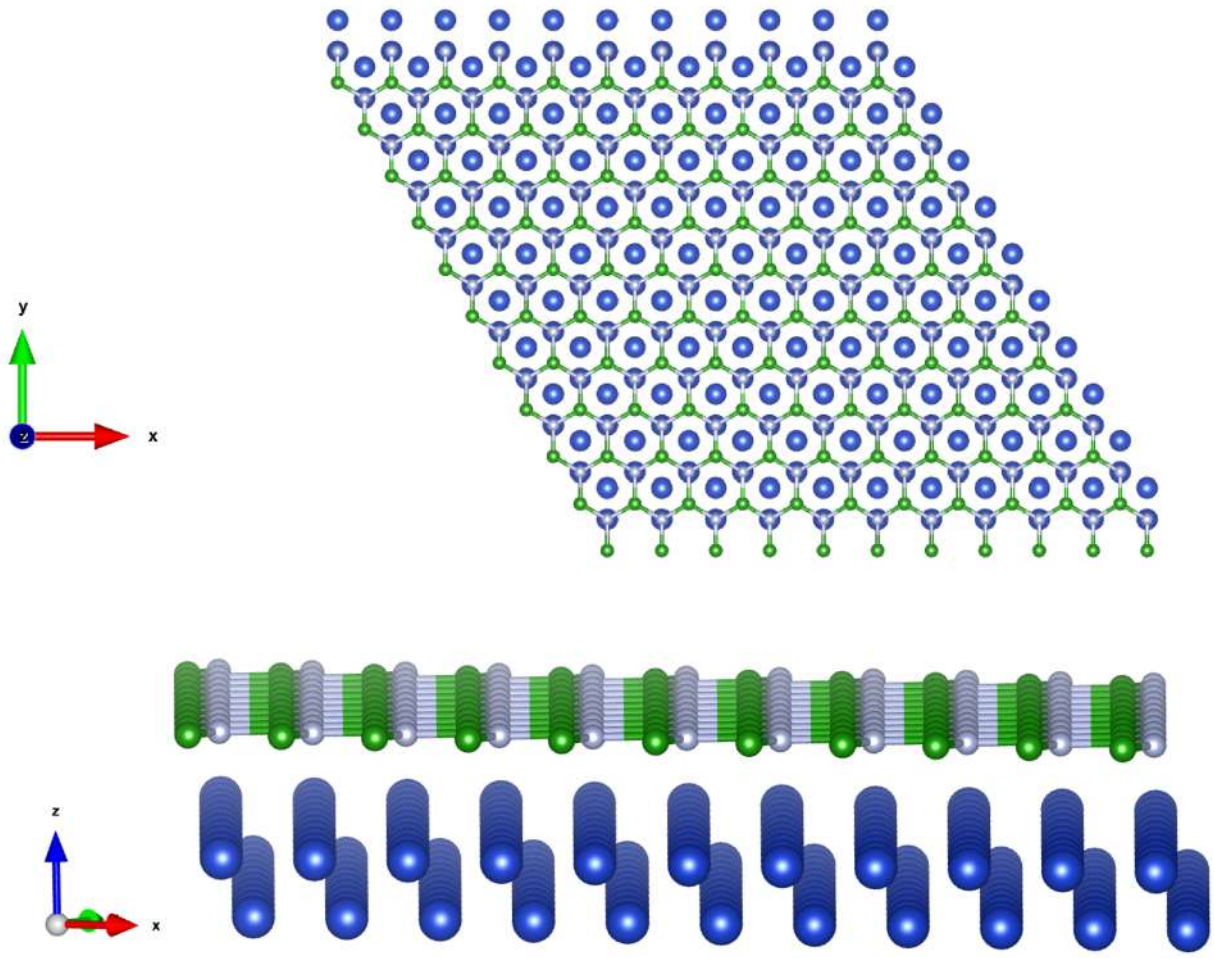

figure S18. Cluster of h-BN/Cu(111) used for simulations showing top (a) and side view (b).

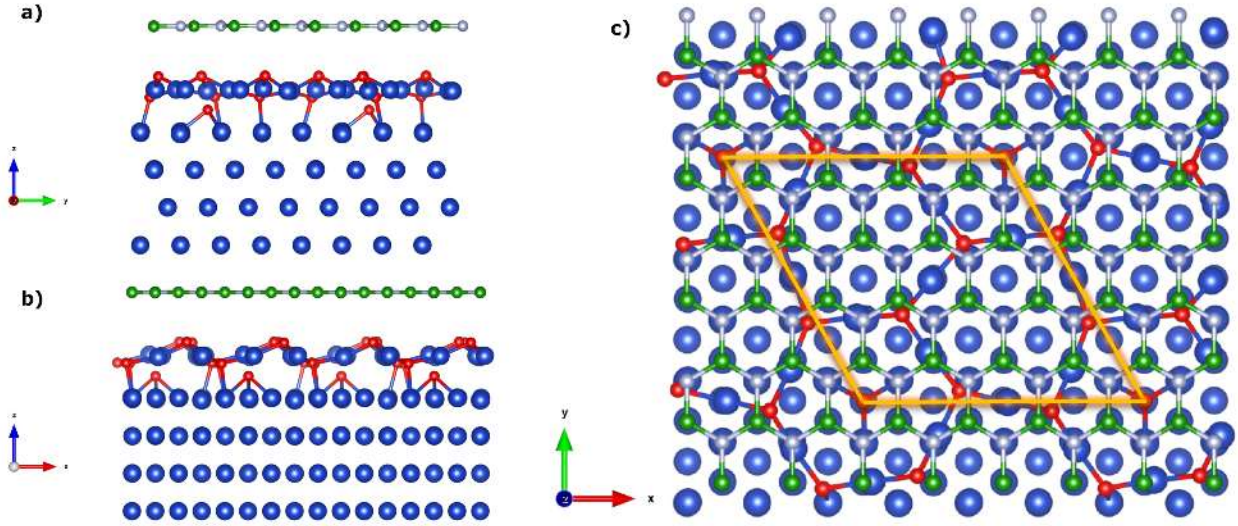

figure S19. Cluster of h-BN/$Cu_{2-x}O$/Cu(111) built first with a commensurate Cu_2O oxide layer above the Cu(111) substrate but below the h-BN, based on the similar structure presented in Yang et al..[45] The system was relaxed using DFT simulations displaying the structure above along the 100 (a), 110 (b) and 111 (c) planes. All simulations of the intercalated oxide utilized this cluster.